DOI: 10.1002/ ((please add manuscript number))

Article type: Review

Electrical Contacts with 2D Materials: Current Developments and Future Prospects

*Saima Batool, Muhammad Idrees, Su-Ting Han, Vellaisamy A. L. Roy and Ye Zhou**

Dr. S. Batool, Prof. Y. Zhou
Institute for Advanced Study, Shenzhen University, Shenzhen 518060, P. R. China.
E-mail: yezhou@szu.edu.cn

Dr. M. Idrees
Additive Manufacturing Institute, College of Mechatronics and Control Engineering, Shenzhen University, Shenzhen 518060, P. R China

Prof. S.-T. Han
College of Electronics Science & Technology, Shenzhen University, Shenzhen, 518060, P. R. China

Prof. V. A. L. Roy
James Watt School of Engineering, University of Glasgow, Glasgow, G12 8QQ UK

Keywords: 2D semiconductors; Electrical contacts; Interface configurations; Numerical analysis; 2D electronics.

Abstract:

Current electrical contact models are occasionally insufficient at the nanoscale owing to the wide variations in outcomes between two-dimensional (2D) mono to multi-layered and bulk materials that result from their distinctive electrostatics and geometries. Contrarily, devices based on 2D semiconductors present a significant challenge due to the requirement for electrical contact with resistances close to the quantum limit. The next generation of low-power devices has already been hindered by the lack of high-quality and low-contact-resistance contacts on 2D materials. The physics and materials science of electrical contact resistance in 2D materials-

based nanoelectronics, interface configurations, charge injection mechanisms, and numerical modeling of electrical contacts, as well as the most pressing issues that need to be resolved in the field of research and development, will all be covered in this review.

1. Introduction

Modern electronics perform incredibly well thanks to the precise control of electric charge flow, which begins with charge injection into an active layer (semiconducting material) through electrical contacts in semiconductor electronic devices. The importance of charge transport was realized fairly early in the development of semiconductor technology, which led to extensive engineering work to change the physical properties of metal electrodes and understand the underlying physical science.[1] Previously, researchers have studied various novel nanostructured materials with advanced properties that can replace conventional materials in terms of electrical, optical, mechanical, and thermal functions. 2D materials-based semiconductors have attracted a lot of attention in recent years.[2]

Nevertheless, a more in-depth understanding of the characteristics of electrical contacts is required if 2D electronics want to transfer from laboratory to real-world application.[1b, 3] Researchers have studied a range of electronic devices that rely on nanotechnology of varied dimensionalities since the early 1990s.[3b] Thanks to advancements in the creation of electronic devices focused on the single- and few-layer form of 2D materials, a group of materials have regenerated with a variety of electronic characteristics.[1a, 1b, 3b, 3h, 4]

Current electronic and optoelectronic devices are mainly based on metal-semiconductor junctions. The Schottky barrier height (Φ_{SB}) indicates the energy barrier for a charge carrier to pass the interface (junction) and is among the most crucial characteristics of the metal-semiconductor junction. It may significantly impact the effectiveness of charge transport and have a consequence on device performance.[5] The Schottky-Mott rule, which was first proposed in the 1930s and regulated by electrostatics throughout all types of issues involving

energy level alignments, may accurately predict Φ_{SB} in a perfect metal-semiconductor junction.[5d, 6] For the properties of the separated material just before the junction formed, X_S and I_S stand for the semiconductor's electron affinity and ionization potential, respectively, and Φ_M stands for the metal's work function. The proposed Schottky barrier heights (for holes and electrons) are $\Phi_{SB,p,}$ and $\Phi_{SB,n}$, respectively (Eq 1, 2). The Schottky-Mott model anticipates the linear dependence of ΦSB on the metal work function with a unified slope.

Yet, the Schottky-Mott model significantly over-predicts the Schottky barrier height. As first observed by Bardeen in 1947, Φ_{SB} is commonly insensitive to Φ_M. In the system, the Fermi level is typically locked to a fixed position within the band gap of the semiconductor, varying little concerning the metals utilized. The interface S variable may be used to determine the strength of Fermi level pinning (FLP) for a specific semiconductor as shown in Eq. 3: [5d, 6]

$$\phi_{SB,n} = \phi_M - X_s \qquad \text{Eq. 1}$$

$$\phi_{SB,p} = I_S - \phi_M \qquad \text{Eq. 2}$$

$$S_{B,p} \quad S = \left|\frac{d\phi_{SB}}{d\phi_M}\right| \qquad \text{Eq. 3}$$

The Schottky-Mott limit is reached when S=1. Regrettably, S is generally far less than 1 for typical semiconductors (0.27 for Si and 0.07 for GaAs). In traditional metal-semiconductor junctions, the Schottky-Mott limit has not been experimentally achieved. The reason is that the Schottky-Mott model is solely dependent on perfect physics and ignores various types of chemical interaction, which are difficult to prevent at the materials' interface. Firstly, surface reconstructions or surface dangling bonds can cause surface states (Bardeen pinning effect or Shockley-Tamm states) within the semiconductor bandgap and cause FLP as a result of incomplete covalent bonds and crystal structure termination. The interface of the contact, where chemical bonds modify their initial energy levels, is rarely an atomically sharp discontinuity between the semiconductor and metal, which brings us to the second point. Large strain can also be created in both crystal lattices by the chemical bonding and inter diffusion between the semiconductor and metal, which changes the band structures and the barrier height. Thirdly,

the standard procedures for device fabrication frequently result in extra chemical instabilities and defect-induced gap states that act as a storage space for charge carriers. The crystal lattice may be damaged by "high-energy" metal deposition processes, which typically include atom/ cluster bombardment and robust local heating to the contact area. In addition, the polymer residue within the interface from the resist development process could cause the deviated barrier height value. Fourth, due to the decaying metallic wave function penetrating the semiconductor, metal-induced gap states are created in the semiconductor-metal junction.

One of the major constraints to the fabrication of functional 2D electrical and optoelectronic devices is the unwanted high contact resistance across 2D semiconductors with three-dimensional (3D) metallic electrodes.[7] In recent decades, improving electrical contacts has emerged as an important research goal. Significant efforts have been made to increase interface current flow and performance characteristics for 2D materials-based electrical devices.[8] Current empirical advancements have shown that a van der Waals (vdW) contact between a metallic electrode and a 2D semiconductor may enhance electrical contact efficiency.[9] This breakthrough brings up new possibilities for investigating how to improve 2D/3D electrical contacts.[10] This necessitates the development of a physical model that encompasses both the material features of 2D semiconductors and the geometrical electrostatic effects in mixed-dimensional nanostructures, while this issue has attracted little consideration in the literature thus far. Generally, effective contact structures incorporate both the 2D material's edge and top surface, owing to the contact's significant surface-to-edge area ratio. As a result, in addition to boosting the edge contacts, overall contact performance could be increased by lowering the tunnel barriers just at the top surface.[11] This might be accomplished through the hybridization of interface metal atoms with 2D semiconducting surfaces. Specific metals can form covalent bonds to 2D semiconducting surfaces, and hence eliminate the vdW gap. For example, InSe/metal,[12] In-Au for WS_2,[13] In for MoS_2 interface,[9a] Cr for WS_2/h-BN heterostructure,[14] Ni for graphene,[15] Ti for MoS_2,[16] Pd for WSe_2,[17] Mo/W for

MoS_2/WSe_2,[18] Ti_2C for MoS_2[19] and graphene/MoS_2.[20] Previous investigations offer a clear explanation of the implementation of Ohmic contact for 2D semiconducting surfaces.[21] In this review, we first discuss the interface configurational geometry between a metal electrical contact and a 2D material. Then the charge-injection mechanisms behind various 2D semiconductors and metal electrical contacts are presented. Moreover, we discuss the electrical contacts resistance, numerical modeling of electrical contacts, and in the end electrical metal contacts materials issues. Several review papers have already summarized the progress of the 2D semiconductor following Ohmic contacts.[8b, 21a] In this review article, we highlight the difficulties in designing high-performance 2D materials-based nanostructure interfaces and discussed potential applications [22] that might make them more widely available, as shown in **Figure 1**. [2n, 21b, 23]

2. Interface configurations

There are two important interface configurations (geometries), top contact and edge contact, which undertake differently between bulk and 2D materials presented in **Figure 2**. Sheer top contacts **(Figure 2b)** can be designed purely via suspending contact between the metal and the 2D material's edges.[24] Nevertheless, due to the atomically thin body of mono or multi-layer 2D material, being able to form a pure edge contact **(Figure 2c)** via classic lithographic strategies is challenging; thus far, only perfect edge-contacted graphene monolayer has been observed.[25] Electrical contacts of 2D semiconductor materials throughout many experiments are a collection of these two configurations.

A basic understanding of the electronic band structure at electrical contacts could be obtained from the band theories. The interpretation of charge-transport methodologies through this potential field would then assist in understanding charge injection. Not all applications require negligible contact resistance, for instance, spintronics is an exception.[26]

2D material's clean surfaces wouldn't produce covalent bonds in contrast to bulk semiconductors **(Figure 3a).** Mostly, the interfaces along metal contacts and any single or multi-layered 2D materials could be shaped via a vdW gap inside the top-contacted configuration (**Figure 3b).**[2h, 3c] The vdW gap in these kinds of top-contact interfaces, as shown in **Figure 3b,** serves as an additional blocking layer for charge carriers before the intrinsic Φ_{SB}. The tunnel barrier on the other hand significantly lowers the charge injection from metals, leading to larger contact resistance. **Figure 3c** presented the metal electrode and 2D multi-layered MoS_2 interface contact along hybridization.

There are various injection mechanisms of metal and 2D semiconductor junctions which are presented in **Figure 4.** The band diagram of conventional electrical metal contact and 2D interface is shown in **Figure 4a.** Making use of edge contacts is one way to avoid the vdW gap. Modeling has revealed that edge contacts to monolayer graphene perform better over top contacts. The edge contacts result in a fairly short bonding distance with relatively strong hybridization than top contacts as demonstrated by density functional theory (DFT). Previous experiments showed that Cr edge contact resistance with graphene is about 150 Ω μm, while the expected value through simulation is 118 Ω μm.[25] Because of the significant conductivity anisotropy that exists in 2D materials between the in-plane and out-of-plane orientations, edge contacts were extremely significant to multi-layered 2D semiconductors.[27] According to the model of top/edge contacts to multilayer graphene,[27a] edge contacts considerably lower the total contact resistance.[27b, 28] Metal contact and 2D multi-layered materials interface with vdW gap and metal contact and 2D multi-layered materials interface with hybridization presented in **Figure 4b-c**. A similar approach, based on a resistance circuit and back-gate screening effect, has been employed to compare top and edge metal-based electrical contact for layered graphene devices.[28] Graphene was patterned underneath the metal-based electrical contact with various perimeter-to-area ratios to theoretically and physically explore the current flow passing through the graphene sheets and edges.[28] According to this model, the edge

contact resistance for each graphene layer is between 150 and 360 Ω μm, which is a low value compared to the tunneling resistances between layers.[29]

However, the majority of contact structures utilize both the 2D material's top surface and edge, with the upper part contributing more since the contact has a significant surface-to-edge-area ratio.[30] Therefore, in addition to improving the edge contacts, the tunnel barrier at the upper surface also needs to be reduced. According to DFT calculations, certain materials, such as Mo/W for MoS_2/WSe_2 [18], Ti for MoS_2 [16b, 31], and Ti_2C for MoS_2.[19] Ni for graphene, [15] Pd for WSe_2[32] can form covalent bonds to 2D semiconductor surfaces and thereby avoid the vdW gap. Under the top contacts, significant hybridization could also alter the properties of 2D semiconductors, especially for a monolayer.[18b] This could change the sheet resistance of semiconductors beneath the contacts (ρ2D contact), and hybridization can also alter the amount of ρ2D contact in both directions. DFT simulations indicate that certain metals like Ti and Mo will produce nonlocalized overlapping states in the initial bandgap of MoS_2[18a] which efficiently converts MoS_2 into a new metallic compound under contact, in this case, ρ2D contact is decreased. However, when the monolayer is incompletely metalized, the localized states may cause the ρ2D contact to rise.

It is important to note that the DFT calculations for significant hybridization instances are predicated on the idea of flawless interfaces. In reality, near-perfect surfaces necessitate annealing as well as the elimination or prevention of surface contaminants including resist residues. For instance, after annealing, the carbon atoms in graphene might dissolve into the contact metal e.g., Co or Ni, forming strong covalent bonds that help to reduce the contact resistance.[33] According to DFT calculations, just the top layer of multilayered transition metal dichalcogenides (TMDs) could be hybridized via top metal-based contacts, removing entirely its vdW gap between the metal and top layer of TMDs.[18b] There is still a vdW gap between the bottom layers. Edge contacts within all layers are therefore preferred to enhance the carrier's injection into the bottom layers. Take MoS_2 for example, [16b, 31] this is true even

though some chosen metals form strong hybridization at interfaces and thereby inhibit the tunnel barrier. The FLP takes place because the binding energy of the metallic surface at interfaces changes into that of the metal-MoS_2 alloy and gap states develop as a result of the weak intralayer S-Mo bonding. The Schottky barrier height (SBH) may be considerably impacted by such phenomena.

In addition to metals, it is also possible to contact 2D semiconductors with other (or identical) low-dimensional elements. At these interactions, "native" chemical bonding is anticipated. For instance, since the carbon family contains both semiconducting and metallic allotropes/structures such as semiconducting carbon nanotube (CNT), and graphene nanoribbon (GNR), scientists can make metallic or semiconducting carbon first, then adjust one side of it to be metallic (or semiconducting). The interfaces between CNT and graphene, graphene and GNR, and the interface between monolayer and multilayer graphene have been theoretically studied.[34]

Such interfaces allow for "seamless" contact between the metallic and semiconducting sides because the bonds there are native sp^2 carbon-carbon bonds. A "seamless" contact for all-graphene circuit architecture was presented and numerically simulated in a recent study. The observed smooth contacts significantly decreased the contact resistance and enhanced circuit efficiency in terms of harmonic distortion, speed, and energy consumption. In these contacts, all the interfaces or junctions between electrical contacts and 2D semiconductors are imagined to begin from a single layer of graphene. Other 2D semiconductors may also benefit from the idea of seamless contacts in certain all-graphene circuit designs **(Figure 3c)**.

Phase engineering was used to fabricate contacts between metallic 1T-MoS_2 and semiconducting 2H-MoS_2 in recent studies.[35] The resultant 0.2 k Ω contact resistance is the lowest ever recorded for this material. Additionally, it is feasible to successively grow metallic and semiconducting TMDs using chemical vapor deposition. To investigate this electrical contact strategy on 2D materials other than graphene, more experimental and theoretical

research is required. Hu and colleagues[36] designed a graphene/h-BN/SnS_2 photodetector which shows a high photoresponsivity. Wang and colleagues[37] demonstrated an ideal vdW interface in coordination with the 2D MoS_2 and metal-based electrical contacts with no interference of chemical interactions. They found that Pd and Pt form clean vdW contacts with MoS_2. They have investigated the interfaces between the evaporated metals (Pd and Pt) with high work function and the 2D semiconductors by scanning transmission electron microscope (STEM), electron energy loss spectroscopy (EELS), and X-ray photoelectron spectroscopy (XPS) as shown in **Figure 5**. The spacing between the Pd and sulfur atoms at the interface was found to be 2.3 ± 0.1 Å. XPS analysis of the Pd-MoS_2 interface showed that the interface is clean with only pristine Pd $3d_{3/2}$ and Pd $3d_{5/2}$ peaks at ~ 340.3 eV and ~ 335 eV visible and no proof of Pd_xS_y or PdS_2 was found as shown in **Figure 5b-c.** The contact resistance of MoS_2 with Pd contacts and WSe_2 with Pt contacts were extracted by the transfer length method (TLM) and shown in **Figure 5i, j.** The hole contact resistance of multilayer MoS_2 with Pd is ~430 kΩ·μm owing to the large Schottky barrier, and the contact resistance of multilayer WSe_2 with Pt is ~3.3 kΩ·μm. The high work function metal contacts present comparable performance to dry transferred metal contacts and these results are much lower than the reported evaporated contact resistances as presented in Figure **5k, l**. Moreover, p-type FETs with vdW interfaces evidence low contact resistance, and their electronic transport performances bring out that the Fermi level is unpinned. The devices exhibited high mobility (~190 $cm^2\ V^{-1}\ s^{-1}$) at ambient temperature following > 10^{-5} $A\cdot\mu m^{-1}$ saturation currents (with an on/off current ratio of 10^7). They also presented an ultra-thin photovoltaic cell with an open-circuit voltage (V_{oc}) of 0.6 V and a power conversion efficiency (PCE) of 0.82% based on n- and p-type vdW contacts.

3. Charge injection

There are two main approaches for injecting charge into the semiconductor as shown in **Figure 6a**. The first mechanism is thermionic emission, and the other is tunneling (field emission)

across the SB, as presented in **Figure 6b-d.** The thermionic emission demonstrates the characteristics of metal vs. semiconductor material with SBH.[5a, 5b] When an inversion layer is located at the interface, carrier combination could potentially be a current-limiting mechanism. This is generally true for semiconductors that have reduced bandgaps which can create an inversion layer very easily, for instance, black phosphorus (bandgap of 0.3 eV).[38] At low doping levels, researchers primarily engage with thermionic emission, while thermionic field emission begins to participate as doping grows as presented with a blue arrow in **Figure 6**. This is comparable to the case of emerging complementary metal-oxide-semiconductor contacts with narrow geometry.[39]

In contrast to the bulk scenario, in which the diffusion area expands both laterally and vertically into the 2D semiconductor, the role of the bands varies only laterally in the metal and 2D semiconductor interface without hybridization. The charges start injecting far away from the contact edge first and meet the flat-band area well before the diffusion region**.** In this instance, predicting the relative influence of thermionic emission and tunneling gets challenging. Since charge injection in 2D semiconductors is highly dependent on the SBH, understanding its significance and knowing how to manipulate it really can enable the process to be improved. The SBH $q\phi_{B0}$ along metal and a semiconductor are given in the ideal situation by the difference $q\phi_{B0} = q(\phi m - \chi)$, [5a] where $q\phi m$ is the metal's work function and $q\chi$ is the semiconductor's electron affinity, q is the elementary electric charge, which is also known as the Schottky-Mott rule.[5a] In practice, the Fermi level at the interface of 2D semiconductor and metal contacts is frequently pinned. This can be calculated by looking at the SBH dependency on ϕ_m (which is given by $S = d\phi_{B0}/d\phi_m$, [5a] with S = 1 corresponding to the ideal case or Schottky limit and $S \approx 0$ corresponding to a pinned Fermi level. The presence of metal-induced gap states causes this pinning at 2D semiconductor and metal contact interfaces.[40] As described in earlier paragraphs, the existence of metal-MoS_2 alloy with a variable work function and the formation

of gaps from the weaker intralayer S-Mo bonding assist in the pinning of metal contacts to 2D semiconductors.

The lower tunability of SBH, therefore, reduces the effectiveness of creating ohmic contact solely by choosing the contact metal. The activation energy in thermionic emission is commonly used to extract the SBH. If we take the example of a FET device, there are two Schottky diodes coupled back-to-back to serve as the source and drain in an SB FET design as shown in Figure 6b. A reverse-biased contact is used on the source side of an n-type SB FET, consuming the majority of the voltage drop and controlling the transistor behavior.

The injection current density through a reverse-biased SB is presented in Eq. 4:

$$J = A^{*}T^{a}_{exp}\left[-\frac{q\phi_{B0}}{k_B T}\right]\left[1-\exp\left(\frac{qV}{k_B T}\right)\right] \qquad \text{Eq. 4 [5a, 41]}$$

A* is nominated as Richardson constant for 2D semiconductor and 3D metal electrodes, Φ_{BO} is nominated for SBH, alpha (α) is equivalent to 2 for bulk 2D semiconductor, V is applied bias, *T* is for temperature, and k_B is Boltzmann constant.[5a, 41] The value of $qV >> k_BT$ so when we simplify Eq. 4 it has been changed into Eq. 5 which was given below

$$J = A^{*}T^{a}\exp\left[-\frac{q\phi_{BO}}{k_B T}\right] \qquad \text{Eq. 5}$$

Mott and colleagues[42] presented the FET device behavior for small gate voltage (Vg) in the sub-threshold regime as mentioned in **Figure 6c-d** and Eq. 6.

$$J = A^{*}T^{a}\exp\left[-\frac{E_A}{k_B T}\right] \qquad \text{Eq. 6}$$

The total activation energy (E_A) in the above equation is = $q\phi_{B0} + E_C^{\infty} - E_C^{0}$ as presented in **Figure 6d**. The E_A is the total activation energy that charge carriers should cross to get into the channel, and $E_C^{\infty} - E_C^{0}$ and the gap between both the conduction and valence band minimum just at the contact boundary interface are presented in **Figure 6d**, due to the upward band bending.

When $V_g = V_{FB}$ (V_{FB} is the flat band voltage) or *V*g is always lesser than V_{FB}, the flat-band condition $E_C^{\infty} - E_C^{0} = 0$ is achieved. Moreover, the activation energy E_A is proportional to Vg:

$$E_A = q\phi_{B0} - \left(1 + \frac{C_{it}}{C_0x}\right)^{-1} \left(V_g - V_{FB}\right) \qquad \text{Eq. 7}$$

where C_{ox} represents gate oxide capacitance and C_{it} represents interface trap capacitance.[43] Additional doping shifts the mechanism from a flat band to a tunneling-contributing phase region as presented in **Figure 6**. The increase in the temperature would vary from the preceding equations in this region, and E_A would no longer rely linearly on V_g. To investigate the SBH, we can find the voltage where E_A stops varying linearly with V_g, which is given by $E_A = q\phi_{B0}$. Das and colleagues[43] used this approach for the extraction of SBH when they used MoS_2 semiconductors with various metal-based electrical contacts. Metal junctions and phase engineering of metal electrical contacts in **Figure 7a** presented that subsurface of MoS_2 forms covalent connections with the Mo contacts, which lowers the SBH.[44]. **Figure 7b** evaluates the Ti contacts which establish a covalent connection with MoS_2, however, the surrounding layers are disrupted, enhancing contact resistance.[45]. MoS_2 and Au contacts interact in a vdW manner, with no change to the carrier mobility there under contact **(Figure 7c)**.[45] The strong interaction of Ag with the MoS_2 layers during the annealing of Ag lowers the contact resistance[46] and the monolayer MoS_2 is changed from the 2H semiconducting phase to the 1T metallic phase by processing with n-butyl lithium in the patterned contact areas before metal deposition, which significantly lowers the contact resistance as presented in **Figure 7d, e**.[47] Liu and colleagues[5d] designed a vdW metal-semiconductor interface. The atomically smooth metal electrodes have been fabricated as well as physically attached to the 2D semiconductors without direct chemical bonding to eliminate bonding disorder as well as defect-induced gap states. **Figure 8a** depicts the fabrication process. To summarize, on a silicon substrate, metal electrodes with varying work functions were initially created.

They could be mechanically separated from the substrate and had an atomically smooth surface. Following that, a mechanical exfoliation approach was used to exfoliate 4 to 20 nm MoS_2. PMMA in this work is a dielectric and critical for maintaining intrinsic electrical characteristics of MoS_2, unlike a traditional MoS_2/SiO_2 contact with several dangling bond states. Following

that, the metal electrodes were transferred over the layers of MoS_2, subsequently resulting in an atomically sharp and clean interface of 2D semiconductor/metal electrode. The benefits of this vdW integration of 2D semiconductors and metal thin-film electrodes might assist in overcoming the limitations of traditional FLP and produce an interface that is close to the ideal physical model.

In aspects of the surface of the semiconductor, Tamm and Shockley state that predominate a covalent semiconductor surface with surface reconstructions or rich surface dangling bonds could be eliminated by the dangling-bond-free surface of the 2D semiconductors. Furthermore, a dangling-bond-free 2D semiconductor surface can avoid developing residues, defects, strains, and the associated defect-induced gap states by physically transferring pre-fabricated metal electrodes instead of using traditional lithography or deposition fabrication techniques. This is evident in cross-sectional transmission electron microscopy (TEM) images, where the deposited metal/MoS_2 interfaces exhibit significant defects, strain, disorder, and metal diffusion **(Figure 8f-h)** in contrast to the transferred metal/MoS_2 junctions (**Figure 8b-d**), which have an atomically clean and sharp interface**.** The interface dipoles and metal-induced gap states can be significantly suppressed by physical contact rather than by direct chemical bonding.

Researchers physically removed the transferred electrode materials from MoS_2 and did electrical measurements to reveal the weak van der walls coupling just at the interface. The core semiconductor is unchanged and maintains its original appearance (**Figure 8e**). In comparison, the metallic electrical contacts with underpinning MoS_2 commonly form a solid chemical bond with the Au-S bondings which was leading to a glassy layer where inter-diffusion and strain predominate. The underlying MoS_2 is destroyed simultaneously with the mechanical peeling of the deposited metal electrodes (**Figure 8i**). Compelling evidence of perfect interfaces also includes retainable integration and separation of metal and 2D semiconductor junctions, whereby two layers nearby maintain their separated states despite specific chemical connections.

Saidi and colleagues[48] investigated the Pd/MoS_2 and Pt/MoS_2 interfaces. They employed semi-local DFT following semi-empirical dispersion modifications. Their results revealed that the metals' adhesion property toward a MoS_2 decreases as metal thickness increases. The effect of electrical contact strain on device characteristics is explained by the d-band model. Even though the d-band model predicts that the interface stability will decrease as more metal layers are deposited, the Pt/MoS_2 contacts exhibit significant anomalous stability on the deposition of two metal monolayers for all examined strains. In contrast, Pd/MoS_2 displays the anticipated results based on the d-band model for unstrained and tensile strained lattices. The results are explained by taking into account the charge decomposition-validated second-nearest-neighbor effect that links MoS_2 with the subsurface metal layers. Furthermore, the significantly high dipole moment and cohesive energy of Pt in comparison to Pd, which also ultimately resulted in a larger charge reaction in the subsurface layers, are attributed as the basis for the differences between Pd and Pt. The electrocatalytic activity of Pt/MoS_2 toward the hydrogen evolution reaction is much higher than that of Pt catalysts with the same Pt loading, as previously demonstrated. Based on the latest findings, it is anticipated either that strain or metal with varying thicknesses may be used to tailor the catalytic performance of MoS_2.

4. Electrical contact resistance

One of the main challenges in the fabrication of 2D electrical and optical devices is the high contact resistance inside the interfaces of 2D semiconductors and metal-based electrodes.[49] Improving electrical contacts through engineering has emerged as a major research goal. In 2D material-based electronics, significant steps have been taken to improve the flow of current via contacts.

According to Banerjee and colleagues[49a], the physics of electron emission differs significantly from that of ordinary 3D materials due to lower dimensionality as well as the unique electronic features of 2D materials. The thermionic emission of charge carriers across

metal/2D semiconductor Schottky contact (**Figure 9a)** is found to be generally governed by a current-temperature (J-T) scaling law,[50] ln (J /T^{β}) = A-B/T, where A and B are material/device dependent parameters, and β = 1 or 3/2 for a vertical or lateral Schottky contact, respectively. For 2D semiconductors, such as atomically thin MoS_2, the thermionic emission is governed by Eq. 8. [50]

$$\mathrm{Jth}(V,T) = \frac{2e\Phi B_0 k_B T}{\pi \tau h^2 \hbar^2 V_F^2}\left(1 + \frac{k_B T}{\Phi B_0}\right)\exp\left(-\frac{\Phi B_0 - \varepsilon F}{k_B T}\right) \quad \text{Eq. 8} \quad [50]$$

Intrinsic SBH is denoted as ΦB_0. V_F is Fermi velocity and its value is 1.1 × 106 m/s for 2D monolayered MoS_2.εF is associated with the Fermi level, the time of carrier injection is τ ≈ 0.1 to 10 ps.[51] In the case of 3D materials, Eq. 8 significantly deviates from the conventional RD thermionic law: $\ln(J_{3D}/T_2) \propto 1/T$.[5a]

Sze and colleagues[5b] presented the Shockley diode equation which would be improved in Eq. 9 based on the detailed-balance principle.

$$J_{2D}(V,T) = \mathrm{Jth}(V,T)\left[\exp\left(\frac{eV}{k_B T}\right) - 1\right] \quad \text{Eq. 9} \quad [5b, 52]$$

The comprehensive 2D Shockley diode equation Eq. 9 signifies 2D electronic systems.[50]

In perspective, for the 3D Shockley diode equation, which is significantly founded on the standard 3D RD thermionic law: $J_{3D}(V, T) = J_{RD}(V, T)$ [exp(eV/k_BT) -1], where $J_{RD}(V, T) = (4\pi m^* k^2{}_B{}^e/h^3)T^2 \exp[-(\Phi_{B0} - \varepsilon_F)/k_BT]$ and $m^* = 0.54m_e$, m_e is the mass of an electron. [53]

$$\frac{\partial I_1(x)}{\partial_x} = -wJ_C(x), \frac{\partial V_1(x)}{\partial_x} = -\frac{-I_1(x)R_{sh\,1}}{W} \quad \text{Eq. 10}$$

$$\frac{\partial I_1(x)}{\partial_x} = wJ_C(x), \frac{\partial V_2(x)}{\partial_x} = -\frac{-I_2(x)R_{sh\,2}}{W} \quad \text{Eq. 11}$$

One of the primary obstacles in the creation of high-performance 2D material-based electronic and optoelectronic devices is the design of efficient electrical contacts with 2D materials. A computational investigation of the electrical contact interface resistance and distribution of the current flow at the interface of the 2D semiconductors and 3D electrical metal contacts has been presented, in addition to various 2D semiconductor materials. Various electrical contact

resistance models have been designed for numerous types of contact interfaces, e.g., 2D/2D metal/semiconductor and 2D/3D metal/semiconductor on behalf of a self-assisted transmission line principle which was linked with a thermionic charge injection and first principles simulation by DFT for 2D semiconductors. It is discovered that the roughness of the contact interface, shown as varying Schottky barrier heights can dramatically reduce the contact resistance in the contact region of MoS_2/metal Schottky electrical contacts (2D/3D). Therefore, roughness management can be utilized to lower contact resistance in 2D materials-based electrical interfaces.

According to experimental findings, the electrical resistance is mainly influenced by the metal contact, the number of layers, and the 2D contact. It is hard to compare the contact resistance values reported in the literature since the available data sets frequently differ by more than one parameter. Despite the availability of results obtained using various metals, it is challenging to determine from this meta-analysis which metal provides the best contact with a given material. The comprehensive literature review concluded that minimal R_C values could be got for MoS_2 as a function of the number of layers as compared to other members of 2D materials.[18b, 35a, 54] There is a clear trend that R_C drops sharply as thickness rises. This should not be unexpected because larger SBs are predicted to result from the wider bandgap in thinner flakes. We can evaluate contact resistances at comparable sheet resistances to make for a better correlation.

The electrical contact resistance at the point of weak-coupling limit is the interface resistivity r_C between the 2D semiconductor and 3D electrical contact have units of ohms per square meter ($\Omega\ m^{-2}$). On the other hand, the sheet resistance of a 2D semiconductor (ρ^{2D}) has units of ohms per square ($\Omega\square^{-1}$).[55] In the case of diffusive contact, charge carrier ions are diffused in a different direction inside the semiconductor and metal interface before being kicked in/or out, and this type of junction (interface) would be described as a 'resistor network' as presented in **Figure 10**. This is referred to as the 'transmission line model'.[55-56] It would provide the following expression (Eq. 12) for contact resistance R_C (in Ω m):

$$R_C = \rho^{2D} r_C \coth\left(l\sqrt{\frac{\rho^{2D}}{r_c}}\right) \qquad \text{Eq. 12}$$

Due to the current saturation, the reliance of R_C on l is nonlinear wherein l is denoted for contact length. If the contact lengths are significantly more than the transfer length denoted as $L_T = \sqrt{\rho^{2D}/r_C}$, where L_T indicates the average distance traveled by an electron or hole in the 2D semiconductor beneath the electrical contact before entering the electrical contact. The contact resistance representation gets $R_C = \sqrt{\rho^{2D}/r_C}$ (in units of Ω m), which is not linked or dependent on contact length. In certain studies, the 'as-measured' resistivity is referenced to as the 'electrical contact resistance' and represented in Ω m^{-2} units. Sometimes for the characterization of electrical contacts, the significant quantity ‘resistance × contact area’ is used, particularly whenever contacts have a considerable contact length dependence l when l and L_T both have identical magnitudes.[56b] Longer electron means free path became the cause of failure of the diffusive approach in graphene, which requires a ballistic approach of contact resistance.

Transition metal dichalcogenides have decreased mean free path which signifies that these materials obey the transmission line model. Hence it is proved that some part of 2D semiconductors resistance under the contact ($\rho^{2D}{}_{contact}$) is utilized in the place of ρ^{2D} in Eq. 12 instead of resistance of the semiconductor channel ($\rho^{2D}{}_{channel}$). However, because of the increased influence of edge contacts, this approach cannot adequately describe metal contacts toward multilayers. Researchers have explored the transfer length in mono and multi-layers of 2D semiconductors (MoS_2) and the number of layers is 2L to 6L.[54a, 54c] L_T value of MoS_2 is about 600 nm[54a] in the monolayer and it is assumed that $\rho^{2D}{}_{contact} = \rho^{2D}{}_{channel}$. Both $\rho^{2D}{}_{contac}$ and r_C can be correctly determined using a more intricate method that is similar to the four-terminal Kelvin resistor scheme.[54c, 55] L_T was approximately 20 to 70 nm for bilayered MoS_2 containing Ti-based electrical contacts and as much as 200 nm for 6-layered MoS_2.[54c] Because of the significant influence of the metal contacts, the hypothesis $\rho^{2D}{}_{contact} = \rho^{2D}{}_{channel}$ collapses in the case of nanostructure channels.

5. Numerical modeling of electrical contacts

Modeling and numerical simulation analysis of contact resistance, with a focus on wear issues, which are coupled with electrical, thermal, and mechanical force, have been carried out.[57] A comprehensive theory of the electrical conductance at the contact surface is established by projecting the continuum model onto the surface and accounting for micromechanical factors. A new model for calculating mechanical and electrical wear is proposed because the wear effect that results from electrical contacts is also a significant feature. In addition, a new friction rule is devised that takes into account surface wear damage.

5.1 Electrical conductance modeling

Various parameters, such as pressure, temperature, and wear, have a considerable impact on the use of electrical contacts. As a result, it is essential to create contact principles that are capable of predicting the resistance of the electrical contacts and wear.[57] Weibenfels and colleagues[57] studied electrical contact resistive models and numerical analysis of linked electrical, thermal, and mechanical fields. They concluded that a pressure-dependent current density at the electrical contact surface must be formulated to reflect these effects. The current density proposed is as follows,

$$\mathrm{J_N} = \mathrm{h_\varphi}(|\mathrm{t_N}|)(\varphi^2 \_ \varphi^1) \qquad \text{Eq. 13}$$

As h_φ express the current transfer function which is dependent on contact pressure denoted as $|t_N|$ and contact voltage denoted as $(\varphi^2 \_ \varphi^1)$. Flux tubes are employed to model the points where contact occurs. These were all equally dispersed and of identical size over the contact surface, as shown in **Figure 11a.** The idea of flux tubes was also used for the thermal interactions which are numerically elaborated as $a_D^{joule} = \varphi_c J_N$ (Joule heating). An initial method of modeling current transfer is conducted by using flux tubes. The impacts of pressure and microscale geometry are taken into account. A unique approach is suggested in which the current density is planned onto the contact surface from the continuum. then the form of the current density occurs at the contact interface.

$$J_N = \sigma(\varphi^2 \_ \varphi^1)/d \qquad \text{Eq. 14}$$

Wherever the σ denoted for mean electrical conductivity has been calculated by the discrete conductivities of the two bodies, first body B^1, $\sigma^{1,}$ and second body B^2, σ^2 correspondingly as shown in Eq. 15.

$$\sigma = \frac{\sigma_1 \sigma_2}{\sigma_1 + \sigma_2} \qquad \text{Eq. 15}$$

The projection is offered by parameter *d*, which must be simulated. To use the flux tube theory, the resistivity of a specific location, also known as spreading resistance *Ri*, is calculated in Eq. *16.*

$$R_i = \frac{1.05}{4\sigma a_i} \qquad \text{Eq. 16}$$

As a result, the spreading resistance is proportional to the radius of the efflux tube's contact spot nominated as a_i. The increased contact resistance R_c could be calculated by connecting the resistivities in parallel

$$\frac{1}{R_c} = \sum_{i=1}^{N_{sp}} 1/R_i = \frac{4\sigma}{1.05} \sum_{i=1}^{N_{sp}} a_i \qquad \text{Eq. 17}$$

Superscript *Nsp* signifies the total number of spots. Ohms law is used for Eq. 18. Moreover, in Eq. 19 A_a is the evident contact area, and the inverse of the diameter is obtained by inserting the above result.

$$\Delta\varphi = R \cdot I = R \cdot J_N \cdot A_a = \frac{J_N \cdot d}{\sigma} \qquad \text{Eq. 18}$$

$$\frac{1}{d} = \frac{J_N}{(\varphi^2 - \varphi^{-1})} = \frac{1}{\sigma R A_a} \frac{4}{1.05 A_a} \sum_{i-1}^{N_{s\rho}} a_i \qquad \text{Eq. 19}$$

Because the asperities diameters are limited, and consequently the pressure is extremely high also for small loads, deformation of the asperities could be supposed, and the following Eq. 20 and 21 holds.

$$\frac{\sum a_i^2 \pi}{Aa} = \frac{|t_N|}{H_v} \qquad \text{Eq. 20}$$

$$J_N = \frac{4\sigma}{1.05\sqrt{A_a \pi}} \sqrt{\frac{|t_N|}{H_V}} \ (\varphi^2 - \varphi^1) \qquad \text{Eq. 21}$$

If current flows, as shown in the following equation for the continuum, additional heat is produced, which is known as Joule heating. This influence can also be seen at the interface of electrical contacts. The heat generated just at the contact interface could be patterned by expressing the continuum's Joule heating onto the contact surface as shown in Eq. 22 and 23.

$$D^s_{joul} = J_N(\varphi^2 - \varphi^1) \qquad \text{Eq. 22}$$

$$= \frac{4\sigma}{1.05\sqrt{A_\alpha \pi}} \sqrt{\frac{|t_N|}{H_v}} (\varphi^2 - \varphi^1) \quad \text{Eq. 23}$$

Joule heating inside the continuum and on the contact interface must always be positive because of the entropy inequality, which would be acceptable because φ^2, $|t_N|$are always greater than zero.

5.2 Modeling of the wear in electrical contacts

$$W = \frac{k F_N \ gT}{H_v} \qquad \text{Eq. 24}$$

At this point, the normal force is denoted by F_N and sliding distance is denoted by g_T. On the other hand, H_v is nominated for Vickers hardness. The k Archard wear factor is nominated for the probability when a particle has been worn away from the surface. It might also be defined as the number of external surfaces that have been worn away per atomic spacing. The progression of wear inside the particular instance of arcing is provided by HOLM.[57]

$$\dot{W} = \frac{\beta}{\gamma} VI \qquad \text{Eq. 25}$$

where *V* denotes voltage, *I* denotes current, the proportionality factor is determined by the latent heat of evaporation, and the factor β implies how many bonds of a molecule are lost, which can vary from 0 to 1 and is determined by the materials used as well as the temperature. Smaller amounts must be employed if every interaction participant acquires a variety of materials. The factor decreases if there is a significant modification in the heat of evaporation within the two materials. When the temperature is extremely high, as it is during an arcing event, the value is

close to one and is typically around 0.2 even when both members are made of similar material. The dissipation, friction, and Joule heating are clear across both mathematical formulas. Consequently, a new method for determining the wear quantity is established.

$$\dot{\mathrm{W}} = \frac{\beta}{\gamma}\mathrm{D}^{\mathrm{s}} \cdot \qquad \text{Eq. 26}$$

The total amount of dissipation resulting from friction coefficient sliding and Joule heating is given by the formula $D^s = D^s_{fric} + D^s_{joule}$. The wear rate in a continuum configuration is shown below for the case of frictional sliding in electrical contacts.

$$\dot{W} = \frac{\beta}{\gamma}u(\phi)F_N \cdot g_T^5 + \frac{\beta}{\gamma}VI \qquad \text{Eq. 27}$$

In which the wear-related surface damage is visible. The magnitude of the relationship agrees well with the data discovered in the literature when the variables of Archard and Holm's wear model are compared to the model that has been proposed.

$$\frac{\mathrm{k}}{\mathrm{H}} = \frac{\beta}{\gamma}\mu(\emptyset) \qquad \text{Eq. 28}$$

The proposed model accounts for the difference with both moderate and severe wear besides changing the coefficient of friction. The damage parameter, which also varies based on dissipation and thus on the quantity of wear, keeps changing the coefficient of friction. Because of the significant heat generated by arcing and the significant portion of worn-off particles that result, a mass transfer feature must be considered.

6. Materials issues

2D materials have been the focus of scientific and engineering research and development for the past decades. Strain engineering in 2D materials has now seen a spike of attention, due to the increasing demand to develop semiconductors at ever-decreasing sizes. Experiments on strain engineering of 2D materials have demonstrated exciting challenges for classical physics as well as intriguing implementations, together with future problems, owing to the atomic nature of 2D materials. Strain engineering has been extensively researched for conventional

semiconductor materials and is currently consistently used during the fabrication process. In some materials, wrinkles and buckle delamination bubbles can co-exist and co-evolve by carefully controlling the degree of induced compressive strain. The localized strain exactly at the peaks of such buckles and creases, where the bending is greatest, is especially important. Recent research has shown that targeted strain can change the optical and electrical properties of 2D materials, such as decreasing the direct band gap in multilayered semiconductors and shifting the absorbance peak by 0.7 eV for black phosphorus.[58] Certain implementations, particularly in strain management, unavoidably rely on mechanical characteristics of both structural response and cognitive functioning. The advantages of the vdW combination of 2D semiconductors and metal thin-film electrodes should help to overcome the constraints of conventional FLP and produce an interface that approaches the perfect physical model. The Tamm and Shockley state typically dominates on a 3D covalent surface of the semiconductor with so many surface representations or dangling bonds that might first be removed by the dangling-bond-free interface of a 2D semiconductor. Instead of using conventional combative fabrication techniques like photolithography or deposition, the physical transference of pre-fabricated working electrodes provides a moderate "limited energy" approach to material incorporation. By doing this, defects, stresses, strain, and the accompanying defect-induced gap states are prevented. The structure of the metal-semiconductor interface must be precisely controlled to produce repeatable and stable electrical properties.

The majority of well-known 2D phase-change substances come from chalcogenides, which have multi-layered bulk structures. The growth-processing-service processes ultimately depend on the phase behavior of 2D materials. It's significant to note that some phase-change 2D materials might be entropically settled down at extreme temps due to high conformational entropy (compositional complexity) or stretching vibrations entropy caused by the presence of soft phonons or powerful lattice anharmonicity, and they might also be steady or thermodynamically stable at ambient temperature.[59] These methods typically do not take into

account the entropy input to phase stabilization, and these materials could not be available in conventional structure forecasting models or from the mining of current crystallography databases. In integrated memory devices, progress toward high-density integration has still been significantly hampered by the lack of large-scale, suitable 2D memory materials.[60] Mechanical exfoliation has been utilized in numerous prior research to create prototype arrays; however, this method is inappropriate for dense integration.[61] The sole alternative is high-temperature chemical or physical vapor deposition. Preliminary efforts using chemical vapor deposition yielded wafer-scale BN and MoS_2 films, but with material quality trade-offs. There are voids, impurities, grain boundaries, and atomic misalignments scattered throughout the films.

Intense research and development have been conducted on improving contact metalization for bulk silicon, germanium, and compound semiconductor devices, and it is still being done. Moreover, due to their high specific surface area ratio (high surface-to-volume ratio and small volume cross-sectional area), the techniques and procedures created for bulk devices should be re-evaluated for nanostructure-based devices. This would be crucial when incorporating nanostructures into high-performance electronics. When other aspects of the device are optimized, the electrode (source and drain) series resistances become a limiting issue. Planar-geometry NiSi has recently been investigated for contact with (111)-oriented Si nanowires, and NiSi-based contacts have been established with a specific resistance of 10^{-8} Ω cm^2.[38] According to this research, Ni reactions with Si nanowires behave differently than they do with bulk Si. Particularly, the crystallographic orientation of nanowires and their capacity to better accommodate strain can result in the stabilization of silicide phases that are typically not seen in thin-film or bulk processes under similar heating conditions.

NiSi is the ideal phase for the aforementioned reasons. Due to the higher Schottky barriers and sheet resistivity, the unique silicide phases may affect the performance of a device and may result in catastrophic device failure if significant internal stress causes extended defect

formation. The orthorhombic Ni_2Si phase, which has the greatest inter-diffusion coefficient, occurs first when a Ni film is placed over a Si substrate and then annealed. The hexagonal θ-Ni_2Si phase occurs at roughly 300°C when Ni-silicide contacts are made with Si nanowires, even though this phase is not visible in the bulk until 800°C. This phase lasts up to at least 600°C despite having a difference in the in-plane bond lengths of over 5% along one direction perpendicular to the metal/nanowire interface; but even so, at 700°C, the silicide forms upwards and whiskers (which might shorten neighboring devices) and a significant number of twins because of the high compressive stress. Epitaxial $NiSi_2$ forms first and is stable up to 700°C, at which point NiSi with low-resistivity forms. However, NiSi is probable to revert to $NiSi_2$ at higher temperatures, possibly leaving a very small process window for the favored phase structure at elevated temperatures. The necessity to probably replace Si with higher mobility semiconductors for elevated performance devices has sparked an active area of research and development in improved contact technology for Ge and group III-V compounds.

The inclusion and activation of dopants is a significant material problem that has already been mentioned in creating metallic contact with nano-materials with controlled electrical properties. The nano-scale depth and spatial resolution required for uniformly doping nanowires are not present in bulk devices doping techniques like a surface modification or solid source in-diffusion, and especially in the case of ion implantation, they also cause severe lattice damage. The self-limiting feature of particular Si surface reactions is used in a recent method to create homogeneous, dopant-containing molecular monolayers on the surface of the nanowire.[38] After being annealed, the dopant diffuses into the main body of the nanowire, and it has been shown that this can result in a dopant concentration of up to 10^{19} cm^{-3} at a depth of 20 nm. The packing density of the dopant precursor (1-propylphosphonate) determines the dopant concentration and results in around 10 times more doping than trioctylphosphine oxide. By annealing carbon nanotubes on titanium at high temperatures, end-bonded contacts, and metal-carbon nanotube interactions have been established, however, these contacts have a significant

Schottky barrier that is roughly equal to half of the bandgap of the nanotubes. It was recently shown that annealing carbon nanotubes in a vacuum at temperatures exceeding 900K with Pt electrodes in contact caused a significant decrease in contact resistivity. Thin graphitic layers on the surface or graphene nanodomains were generated to boost the electronic overlap between the carbon nanotube and metal, thereby increasing the area of the contact.

Even though there have been several studies on the intercalation of 2D materials for versatile applications, there are still some problems that necessitate further fundamental investigation in this quickly developing field.[62] Additionally, choosing the host and guest combination for intercalation chemistry is not sufficiently apparent to achieve intentional structural alteration. Therefore, a more thorough investigation of the in-situ mechanism is required to determine the actual structural modifications that occur during the intercalation. Comparative trials employing various intercalation schemes can help to achieve this.[63] 2D TMD's three crystalline phases are presented in **Figure 12a.** [64] The STS images of 2H, 1T and 1T′phase measurements of MoS_2 can be seen in **Figure 12b-d**.[65]

By using the chemical vapor deposition approach, Lukowski and colleagues [66] reported the creation of a flower-like MoS_2 nanostructure with a high density of exposed edges directly on a graphite substrate. After that, 2H-MoS_2 nanosheets are doped in n-BuLi solution (6 to 48 hours at 60 °C) to transform into the 1T-MoS_2 phase. This finding opens up intriguing possibilities for research into nanomaterials used to inject charges into other nanostructures. One of the major hurdles is the creation of high-efficiency, cost-friendly, and widespread intercalation technologies. Furthermore, most of the intercalated 2D materials lack stability in the air. Therefore, stability is a major concern, particularly whenever sensitive intercalants such as alkali and alkali-earth metals are utilized.

For the development of successful contact engineering strategies, a basic understanding of 2D interface contact physics, comprising interfacial energy level alignments, transfer length, and FLP is required. Firstly, the easiest technique is to adjust the energy levels of interfaces to cut

down the Schottky barriers by carefully choosing 2D materials and metals with matched energy bands. Moreover, due to interfacial FLP and orbital hybridization in particular 2D/metal systems, this approach invariably fails. Secondly, new doping approaches which are motivated through degenerated Si-based devices are also suited to 2D materials-based devices. The dope 2D electrical contacts used these approaches to narrow Schottky barriers and remove FLP. TMDs, especially those with high polymorphism phase engineering from 2H to 1T can metalize the metal electrical contact. It is crucial to achieving air-stable metallic 2D contacts for both phase engineering and contact doping. Thirdly, another effective way for producing atomically flat surfaces at the contact and altering the interfacial energy level alignments is to insert several buffering layers in the middle of 2D materials and electrical metal contacts. Fourth, the FLP-free electrical contacts are designed via 2D materials-based active layers and metallic electrical contacts having vdWs bonding. The FLP-free contact can also be created without bringing defects, interfacial stresses, or residues during the manufacture of the device. Fifth, the edge contact also enhances robust orbital hybridization and narrowing the Schottky barrier and facilitates the carrier injection characteristic in 2D materials and metal electrical contacts. There is no lateral overlapping in the 2D semiconductors and metal electrical contacts in this contact geometry. Moreover, the scaling down of 2D electronic devices can be made easier.[67]

The influence of a substrate on electrical contact conductance is especially interesting for electronic systems[68] and electrical contacts.[69] 2D materials have already been intensively researched due to their exceptional physical and chemical characteristics.[70] The features of 2D materials based electrical contacts, on the other hand, are directly connected to the substrate and extrinsic strain. As a result, the strain may be affected by the type and shape of the substrates, hence influencing the properties of 2D materials.[71] The substrate's lattice structure and orientation could be modified to control the optical, electrical, electromagnetic, and chemical stability.[72] Several substrates including rough, flexible and elastic substrates, have been used. In the research fields of magnetic detectors, optoelectronic devices and electrochemical

hydrogen absorption, etc. methods for creating strain and manipulating the materials' properties have been introduced. Furthermore, in addition to strain and substrate, a variety of other factors may influence material qualities. As a result, there still exist difficulties in accurately analyzing and designing substrate shapes for managing the properties of materials. Moreover, because of the variety of substrate materials, understanding the influence of substrate materials and substrate strain on the attributes of 2D electrical contacts is an important issue that must be solved. As a result, a precise understanding of the link between structure and efficiency is required. In principle, substrates strain management provides an effective way of managing material properties while also diversifying its prospective applications. MoS_2 FETs with perched substrates, graphene magnetic detectors with terrace substrates, and quantum light sources with patterned substrates have been investigated. In addition, high-performance photodetectors[73] and wearable devices based on flexible substrates have been developed.[74] These devices can help with the application and development of 2D materials in microelectromechanical systems.

Flexible or soft electronics,[75] that offer the advantages of lightweight, low cost, large area, and durability, have indeed been created for a variety of purposes, including paper-like electronics sensors, rollable solar cells, electronics skins, and so on. During manufacturing and usage, the systems may experience one-time or recurring large deformation. Hu and colleagues [68] chose three systems to study the substrate effect, from no substrate and elastic substrate to rigid substrate. The goal of this research was to determine the impact of the substrate on the graphene contact conductance as determined via an atomic force microscope. At the constant applied force, the current rises as follows: rigid substrate < elastic substrate < no substrate. They showed that the substrate support affects graphene/tip contact conductance via substrate elasticity, which dictates variability of interatomic distances in the contact and contact size, that adds to interface resistivity. Until now, most flexible electrical devices are organic/inorganic

hybrids with various materials and designs.[76] There is still a long way to create fully flexible systems based on 2D electrical contacts.

7. Prospects

Natural curiosity and scientific passion have been the main forces behind 2D electronics research. Therefore, it may not be proper to evaluate their technical competence. At this moment, it seems inappropriate to predict on whether and when these 2D materials will rule the semiconductor market. Fundamentally speaking, these 2D semiconductors can replace transitional semiconductor materials because of their atomically thin structure, which allows for rapid scaling and has a specific benefit for energy efficiency. However, a long way still needs to be travelled before 2D semiconductors can be produced on a wafer scale at temperatures suitable for back-end processing without sacrificing their excellent quality and meanwhile ensuring low defect densities.

Significant advancements have been made in producing highly scaled FETs with sub-10 nm gate lengths and reducing the contact resistance of 2D FETs in response to these unsolved issues. Diverse contact methods need to be used and tested on large-scale fabrication. Contact length scaling issues can be resolved by increasing the inter facial resistance and sheet resistance beneath the contacts. Another vital matter that must be considered is the parasitic capacitance that the structure and geometry cause. How to make low-resistance contacts for top-gated 2D FETs is a significant topic that has not yet been investigated a lot in the literature. The lowest contact resistance is attained in the ON state of a back-gated FET because the global back gate controls the carrier concentration beneath the contact. However, degenerate doping of the 2D material beneath the contacts appears to be required since there is no contact gating in top-gated FETs. Additionally, high-performance p and n-type FETs are required for complementary circuit implementation, which needs the seamless injection of both holes and electrons into the appropriate bands of the 2D semiconductor. Due to its ambipolar conduction, WSe_2 is presently

one of the most promising materials demonstrating p and n-type performance. Nevertheless, WSe_2 devices are still constrained by high contact resistances. It is technically feasible to have multiple TMDs for n-type and p-type, but doing so will be very complex and undesired.

The true capacity of 2D semiconductors can only be achieved with strong electrical contacts. The atomic thickness and pristine surfaces make it 2D materials difficult to reduce the contact resistance. Novel experimental approaches and theoretical models which are suited for 2D material must be developed. Only with strong electric contacts could 2D semiconductors be used to their full potential. It is challenging to lower the contact resistance of 2D materials to their atomic-scale thickness and flawless surfaces. It is essential to develop fresh theoretical frameworks and empirical evidence that are tailored specifically to the 2D semiconducting material. This problem's solution has come a long way in recent years. There are a few methods to make high-quality electrical contacts, but achieving seamless electrical contacts where natural chemical bonds allow for significantly simpler charge transport and subsequently lower contact resistances might be most practical. Examples include the preservation of sp^2 hybridization at graphene-graphene nanorod junctions or the use of metallic TMDs as covalent contacts for semiconducting TMDs. Moreover, specific traits of semiconducting materials like atomic flaws and constituent elements can have an important impact on the device's electrical properties. Spintronics, a separate study field that focuses entirely on managing contact resistance would become progressively crucial for TMDs.

In summary, we have discussed the physics and materials science of electrical contact resistance in 2D materials-based nanoelectronics, interface configurations, charge injection mechanisms, and numerical modeling of electrical contacts, as well as the most pressing issues that need to be resolved in the field of research and development in this article.

Acknowledgments

We acknowledge the grants from National Natural Science Foundation of China (Grant No. 61974093), the Science and Technology Innovation Commission of Shenzhen (Grant No. RCYX20200714114524157 and JCYJ20220818100206013), NTUT-SZU Joint Research Program, and the Natural Science Foundation of SZU.

Received: ((will be filled in by the editorial staff))

Revised: ((will be filled in by the editorial staff))

Published online: ((will be filled in by the editorial staff))

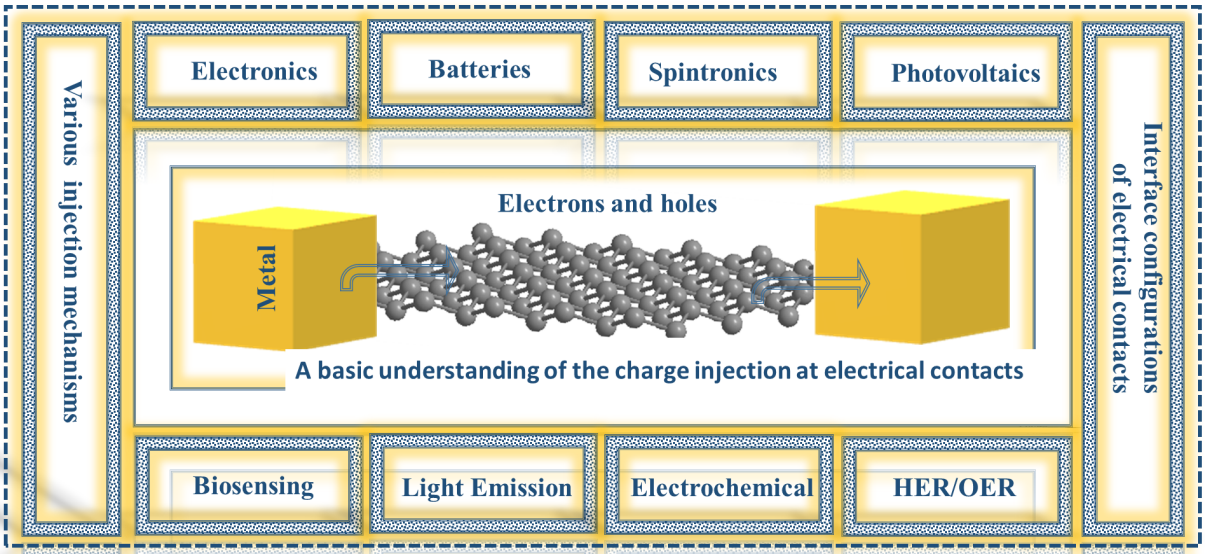

Figure 1. Schematic diagram presents the application of typical electrical contacts and various injection mechanisms in various devices.

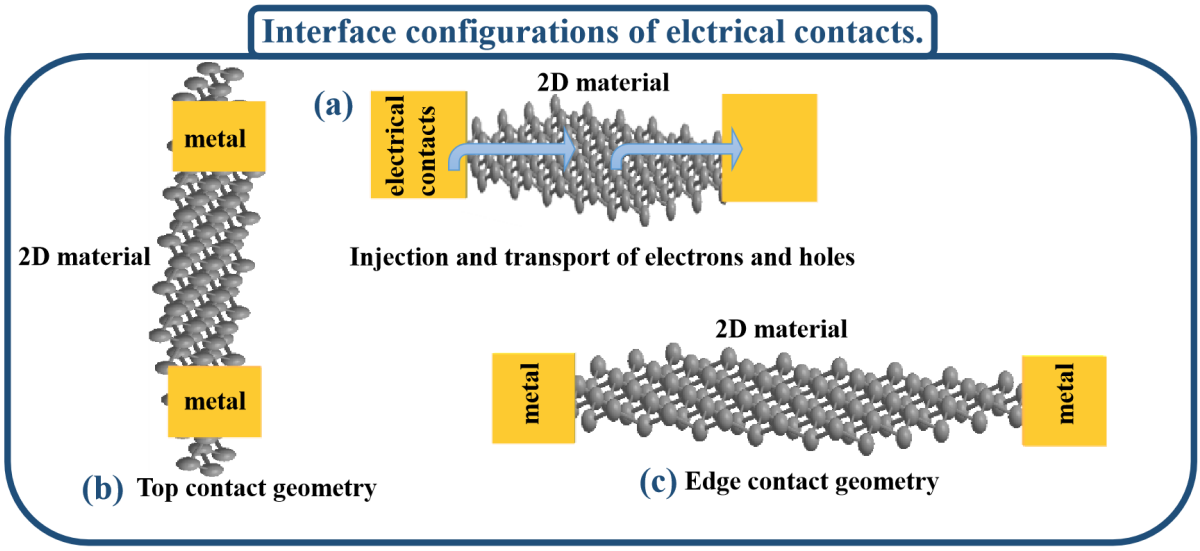

Figure 2. Interface configurations of 2D materials-based electrical contacts. (a) The injection and transport of electrons and holes inside 2D materials and their electrical contacts. (b) Top contact geometry and (c) edge contact geometry.

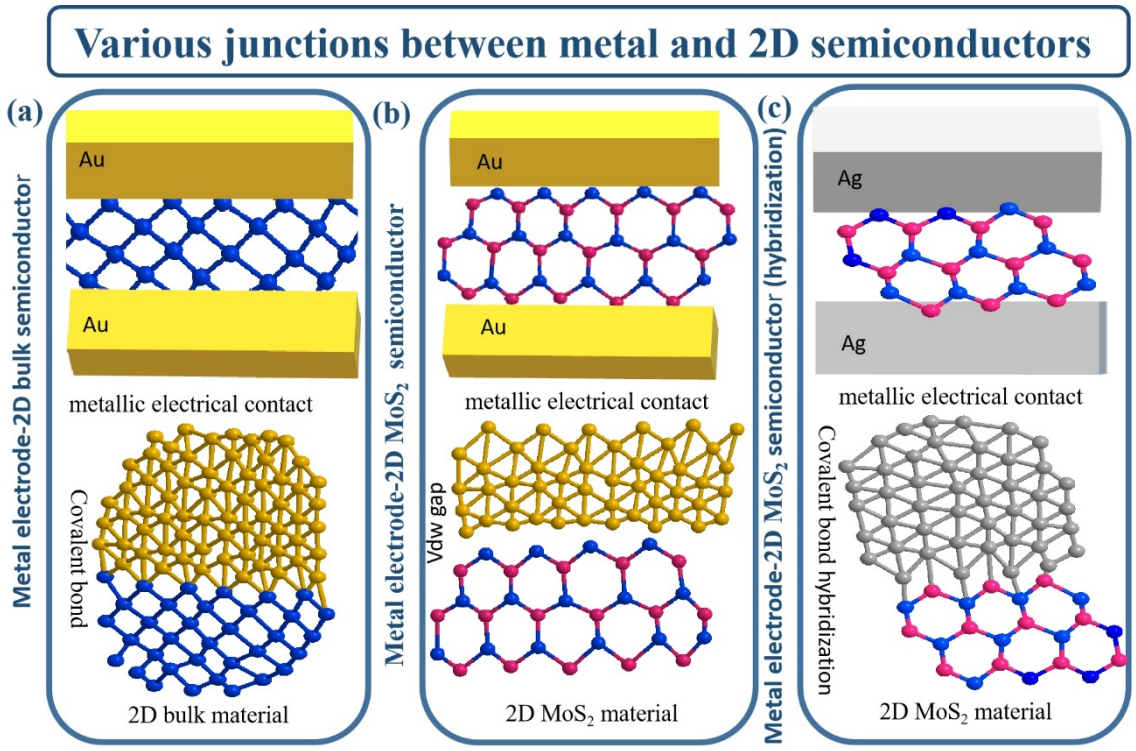

Figure 3. Various junctions between metal and 2D semiconductors. (a) Metal electrode and bulk 2D material-based interface contact. (b) Metal electrode and 2D multi-layered MoS_2 interface along vdW gap. (c) Metal electrode and 2D multi-layered MoS_2 interface contact along hybridization.

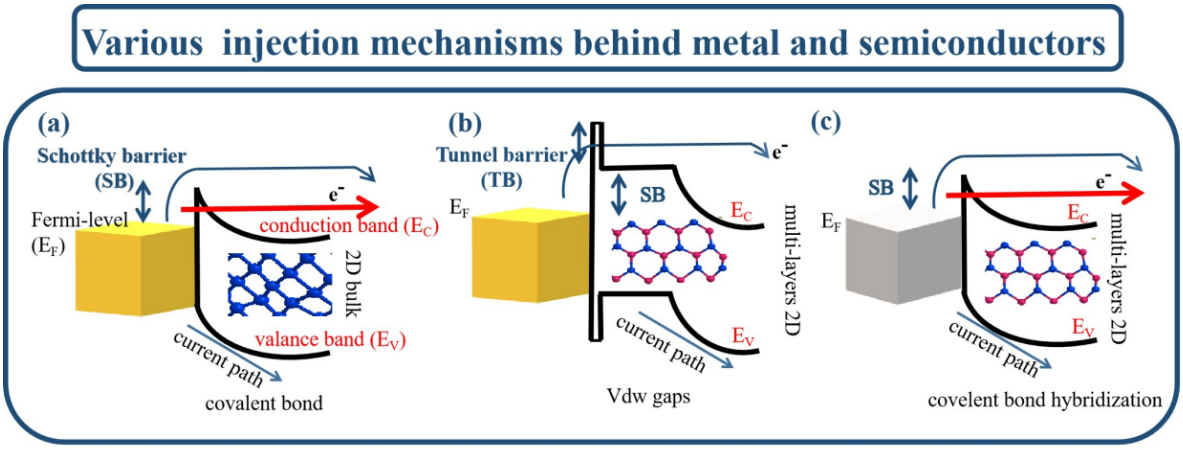

Figure 4. Various injection mechanisms of metal and 2D semiconductor junctions. **(a)** Band diagram conventional electrical metal contact and 2D bulk interface. **(b)** Metal contact and 2D multi-layered materials interface with vdW gap. **(c)** Metal contact and 2D multi-layered materials interface with hybridization. Reproduced with permission. [49b] Copyright 2015, Springer Nature.

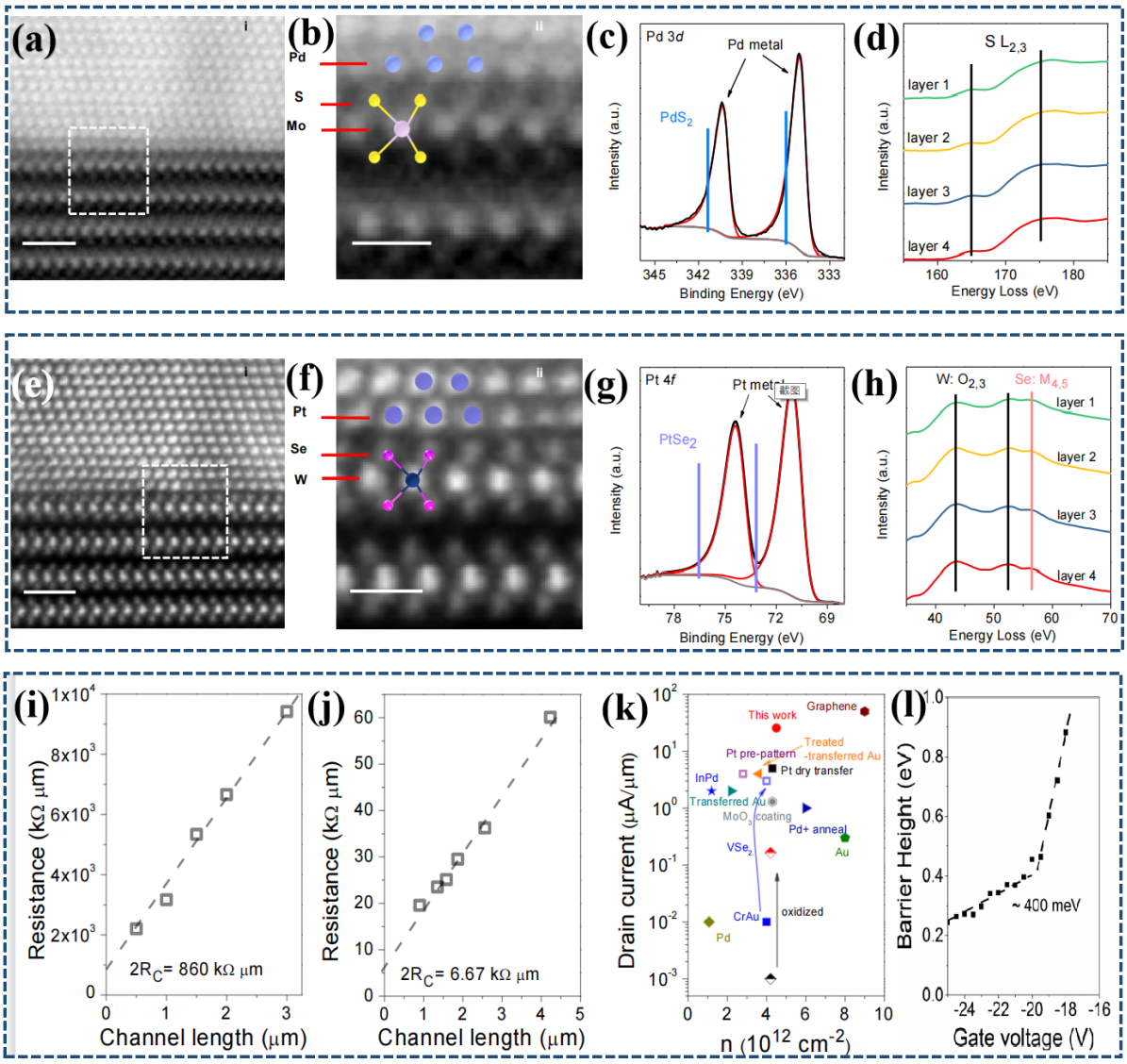

Figure 5. (a) Cross-sectional STEM image shows that the Pd forms clean vdW contacts with MoS_2. (b) The spacing between the sulfur and Pd atoms. (c-d) XPS Spectra of Pd-MoS_2. (e) Cross-sectional STEM of the Pd forms clean vdW contacts with few-layered WS_2 (f) The spacing between the sulfur and Pd atoms at the interface was found to be 2.3 ± 0.1 Å, (g-h) XPS Spectra of Pd-WS_2 based device. (g, h) TLM results of multilayer MoS_2 and WSe_2 with Pd electrodes. (i, j) Comparison of drain current contact resistance of WSe_2 FETs with values reported in the literature using different methods.[37] Reproduced with permission.[37] Copyright 2022, Springer Nature.

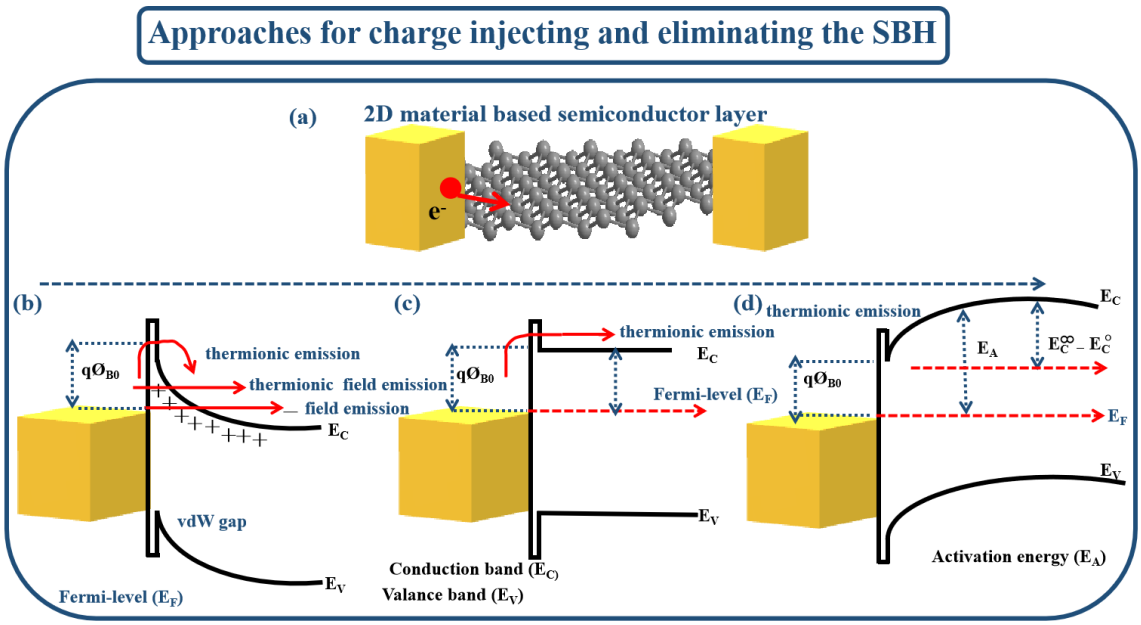

Figure 6. (a) 2D materials-based charge injecting mechanism. (b-d) The first mechanism is thermionic emission, and the other is tunneling (field emission) across the SB. Reproduced with permission. [49b] Copyright 2015, Springer Nature.

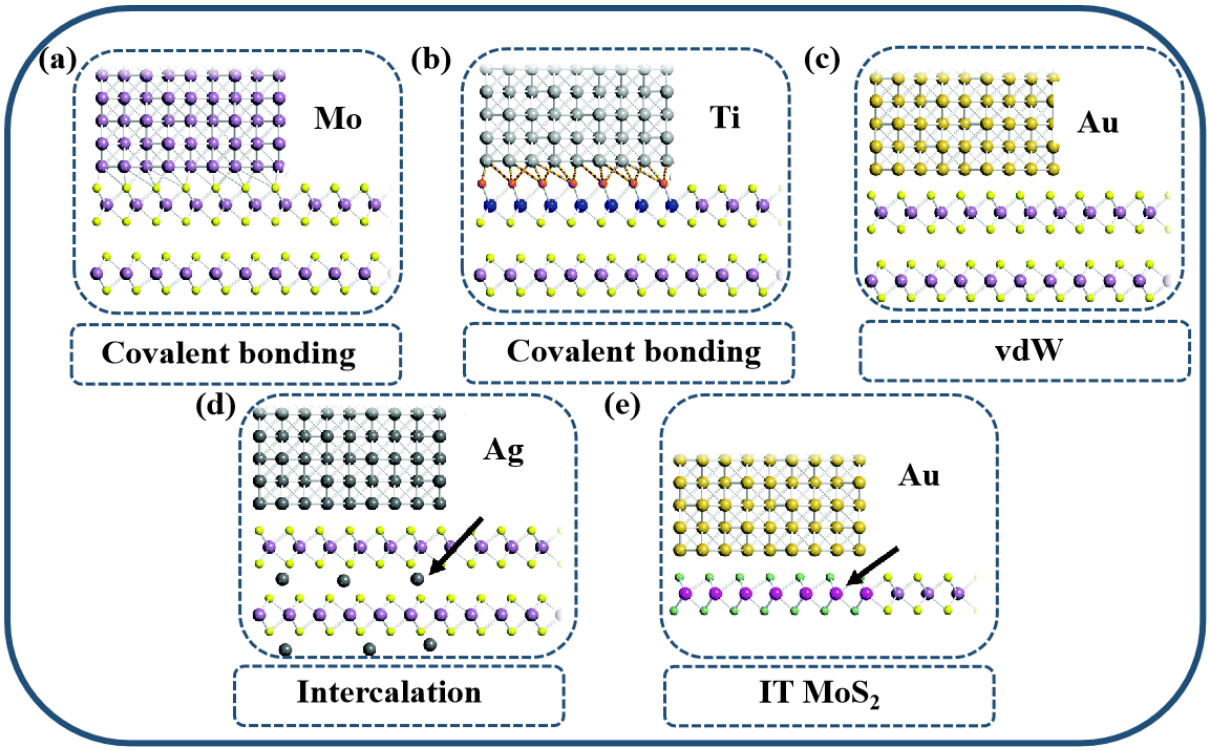

Figure 7. Metal junctions and phase engineering of metal electrical contacts: (a) The subsurface MoS_2 forms covalent connections with the Mo contacts, which lowers the SB height.[44] Reproduced with permission.[44] Copyright 2014, AIP. (b) Ti contacts similarly establish covalent connections with MoS_2, however, the surrounding layers are disrupted, enhancing contact resistance.[45] Reproduced with permission.[45] Copyright 2014, American Chemical Society. (c) MoS_2 and Au contacts interact in a van der Waals manner, with no change to the carrier mobility there under contact.[45] Reproduced with permission.[45] Copyright 2014, American Chemical Society. (d) The strong interaction of Ag with the MoS_2 layers during the annealing of Ag (250 or 300 °C) lowers the contact resistance.[46] Reproduced with permission.[46] Copyright 2017, AIP. (e) The monolayer MoS_2 is changed from the 2H semiconducting phase to the 1T metallic phase by processing with n-butyl lithium in the patterned contact areas before metal deposition, which significantly lowers the contact resistance.[47] Reproduced with permission.[47] Copyright 2014, Springer Nature. Reproduced with permission.[48] Copyright 2014, AIP.

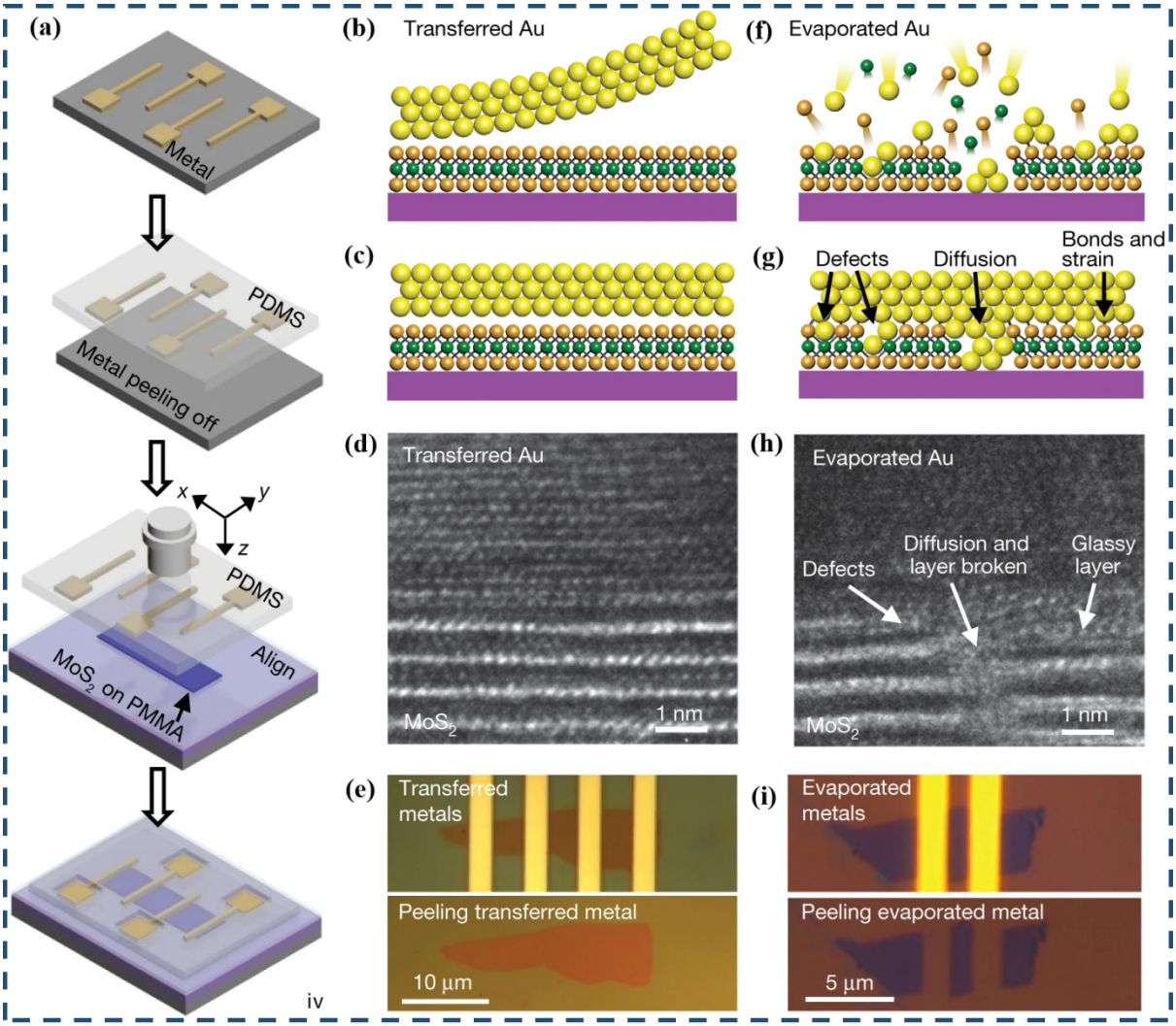

Figure 8. (a) Metal-semiconductor interface of vdW incorporation is shown graphically: (i) Deposition of metal on the substrate surface; (ii) Metal peeling off; (iii) Transferring the metal electrode; and (iv) Transferred metal electrode on top of MoS_2. (b-e) Metal-semiconductor interfaces with transferred Au electrode upon the top of MoS_2. (f-i) Metal-semiconductor interfaces with evaporated Au electrode upon the top of MoS_2.[5d] Reproduced with permission.[5d] Copyright 2018, Nature.

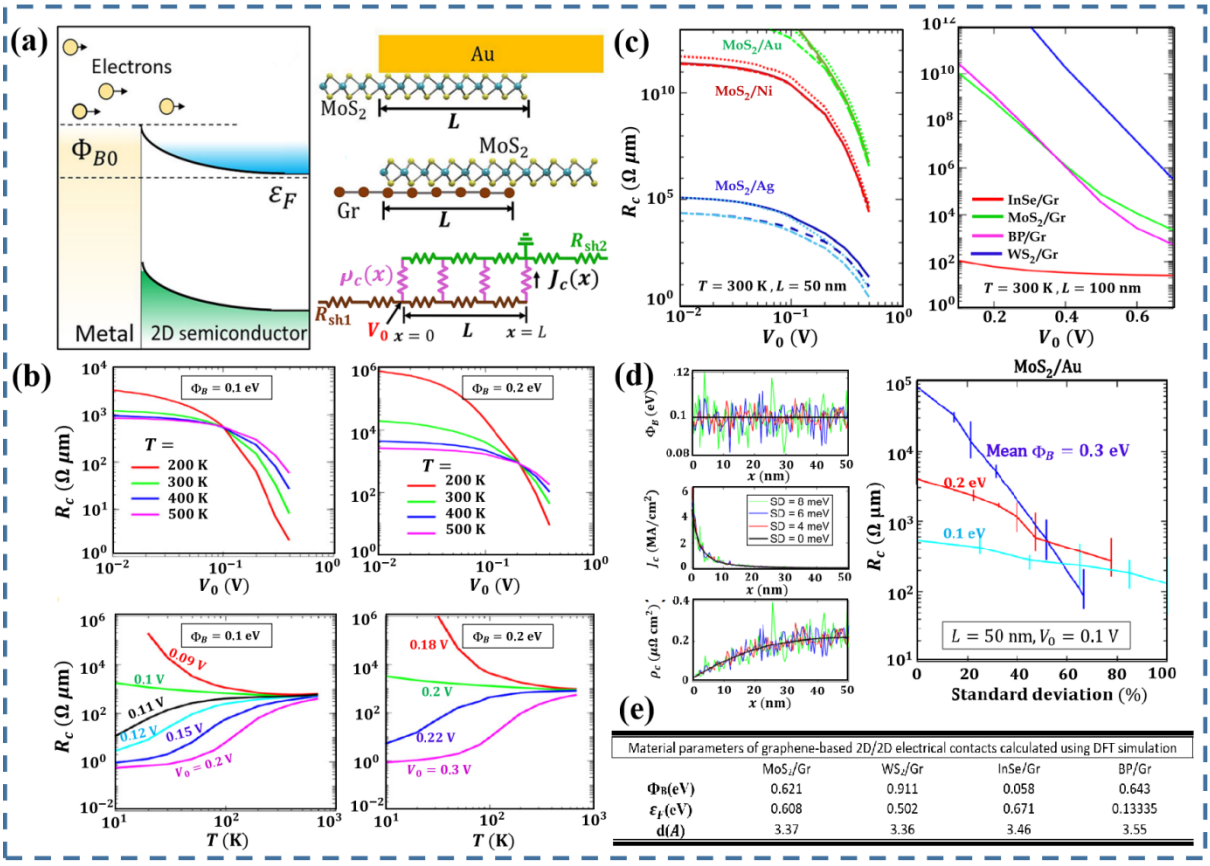

Figure 9. (a) Right: energy band diagram of 2D semiconductor and metal-based electrical contacts. Left: moderate overlap of electrical contact of monolayered MoS_2 and gold, then graphene and MoS_2 following the model of transmission-line. (b) Contact resistance (Rc) as a function of V_0 (applied voltage) at various T values (B = 0.1 and 0.2 eV). Rc as a function of T for various values of V_0 (B = 0.1 and 0.2 eV). (c) Rc concerning applied voltage (V_0) in the presence of various Schottky electrical contacts. (d) The monolayer MoS_2/Au interface at various standard deviation (SD) values gives specific values of electrical contact resistance. The Schottky barrier height unevenness is indicated as Φ_B which gives current density as Jc(x), and it gives a specific contact resistivity at interfaces of electrical contacts. (e) DFT modeling was used to calculate the material characteristics of graphene-based electrical contacts.[49a] Reproduced with permission.[49a] Copyright 2020, AIP

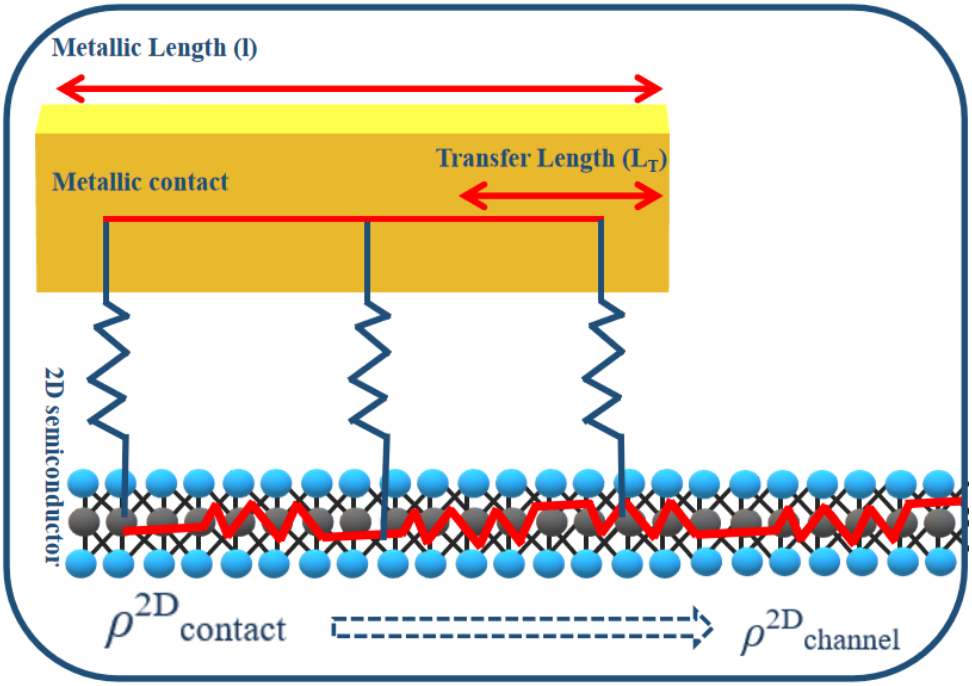

Figure 10. The model is represented by the resistor system. $\rho^{2D}_{contact}$ and $\rho^{2D}_{channel}$ presents the semiconductor layer resistance in the channel and underneath the contact, accordingly.

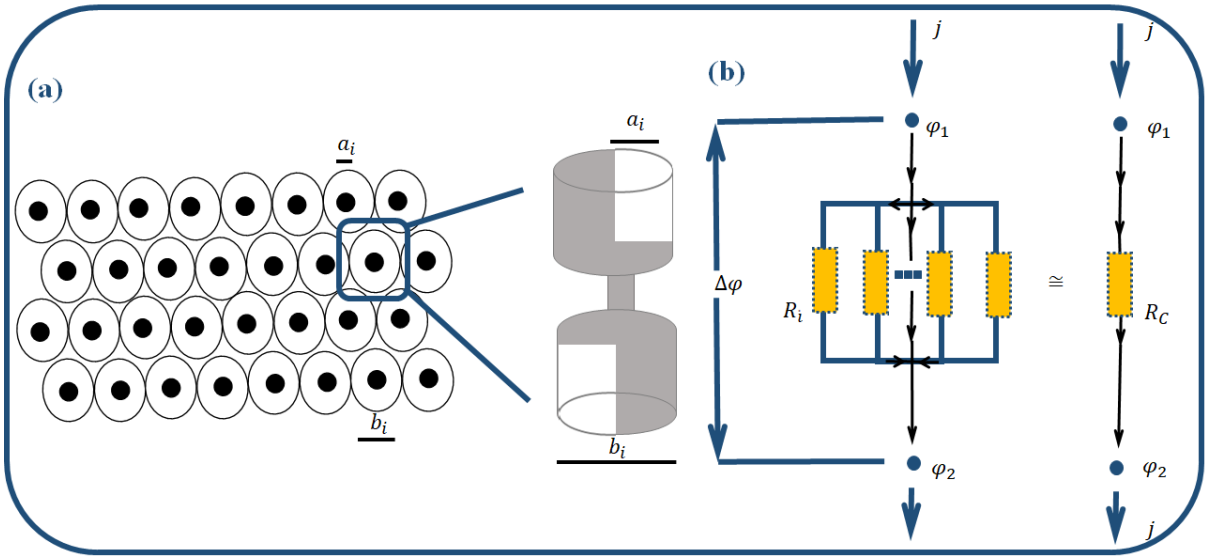

Figure 11. (a) Reflux tube modeling of the electrical contact interface. (b) Single electrical contact resistance is used to represent single constriction resistances. Reproduced with permission. [57] Copyright 2009, Springer Nature.

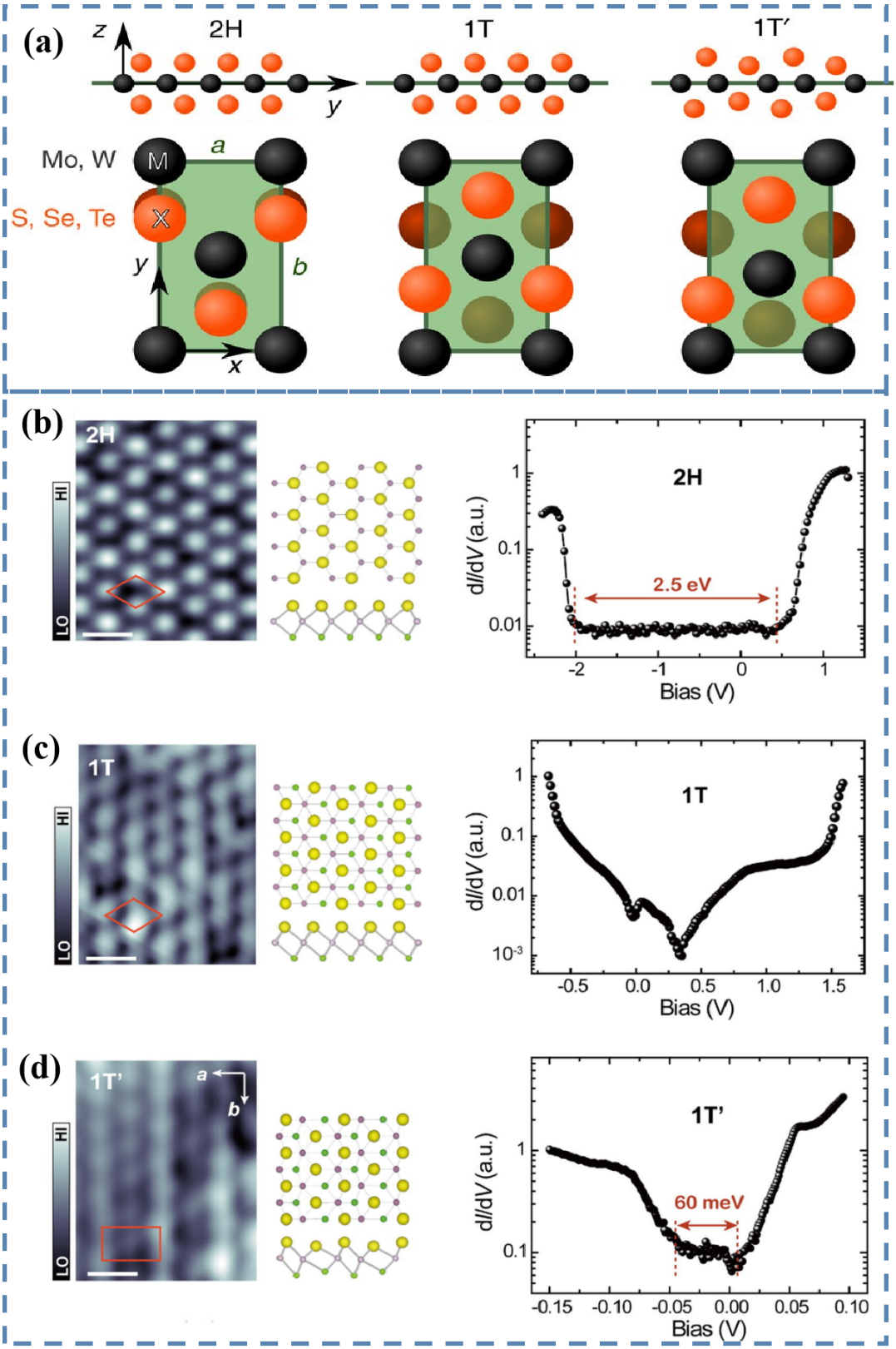

Figure 12. (a) Three crystalline phases of 2D TMDs.[64] Reproduced with permission.[64] Copyright 2014, Springer Nature. (b) STS image and measurements of MoS_2 2H phase. (c) STS images and measurements of 1T phase. (d) STS image and measurements of MoS_2 $1T^-$ phase.[65] Reproduced with permission.[65] Copyright 2019, Elsevier.

References

[1] a) S. V. Suryavanshi, B. Magyari-Kope, P. Lim, C. Mcclellan, E. Pop, *Nature Materials* **2021**, *11*, 1195; b) J. Yao, K. J. Koski, W. Luo, J. J. Cha, L. Hu, D. Kong, V. K. Narasimhan, K. Huo, Y. Cui, *Nature Communications* **2014**, *5*, 1; c) Y. Zhang, X. Rui, Y. Tang, Y. Liu, J. Wei, S. Chen, W. R. Leow, W. Li, Y. Liu, J. Deng, *Advanced Energy Materials* **2016**, *6*, 1502409; d) M. Zhao, J. Su, Y. Zhao, P. Luo, F. Wang, W. Han, Y. Li, X. Zu, L. Qiao, T. Zhai, *Advanced Functional Materials* **2020**, *30*, 1909849

[2] a) F. Bonaccorso, Z. Sun, T. Hasan, A. Ferrari, *Nature Photonics* **2010**, *4*, 611; b) A. Carvalho, M. Wang, X. Zhu, A. S. Rodin, H. Su, A. H. Castro Neto, *Nature Reviews Materials* **2016**, *1*, 1; c) H. C. Chang, C. L. Tu, K. I. Lin, J. Pu, T. Takenobu, C. N. Hsiao, C. H. Chen, *Small* **2018**, *14*, 1802351; d) M. Chhowalla, D. Jena, H. Zhang, *Nature Reviews Materials* **2016**, *1*, 1; e) S. Cui, Pu, H., Wells, S. A., Wen, Z., Mao, S., Chang, J., Hersam, M. C., Chen, J. , *Nature Communications* **2015**, *6*, 8632; f) *Nature Communications* **2015**, *6*, 8632; g) A. D. Franklin, *Science* **2015**, *349*, 2750; h) A. K. Geim, I. V. Grigorieva, *Nature Communications* **2013**, *499*, 419; i) D. Hanlon, C. Backes, E. Doherty, C. S. Cucinotta, N. C. Berner, C. Boland, K. Lee, A. Harvey, P. Lynch, Z. Gholamvand, *Nature Communications* **2015**, 1; j) G. Konstantatos, *Nature Communications* **2018**, *9*, 1; k) M. Lanza, Q. Smets, C. Huyghebaert, L.-J. Li, *Nature Communications* **2020**, *11*, 1; l) L. Li, Y. Yu, G. J. Ye, Q. Ge, X. Ou, H. Wu, D. Feng, X. H. Chen, Y. Zhang, *Nature Nanotechnology* **2014**, *9*, 372; m) F. Bonaccorso, Z. Sun, T. Hasan, A. Ferrari, *Nature Photonics* **2010**, *4*, 611; n) H. Zhang, *ACS Publications* **2018**, *118*, 6089.

[3] a) W. Michailow, P. Spencer, N. W. Almond, S. J. Kindness, R. Wallis, T. A. Mitchell, R. Degl'Innocenti, S. A. Mikhailov, H. E. Beere, D. A. Ritchie, *Science Advances* **2022**, *8*, 8398; b) K. S. Novoselov, A. K. Geim, S. V. Morozov, D. Jiang, Y. Zhang, S. V. Dubonos, I. V. Grigorieva, A. A. Firsov, *Science* **2004**, *306*, 666; c) K. S. Novoselov, A. Mishchenko, A. Carvalho, A. C. Neto, *Science* **2016**, *353*, 9439; d) Q. H. Wang, K. Kalantar-Zadeh, A. Kis, J. N. Coleman, M. S. Strano, *Nature Nanotechnology* **2012**, *7*, 699; e) S. Haigh, A. Gholinia, R. Jalil, S. Romani, L. Britnell, D. Elias, K. Novoselov, L. Ponomarenko, A. Geim, R. Gorbachev, *Nature Materials* **2012**, *11*, 764; f) D. Rhodes, S. H. Chae, R. Ribeiro-Palau, J. Hone, *Nature Materials* **2019**, *18*, 541; g) D. Akinwande, C. Huyghebaert, C.-H. Wang, M. I. Serna, S. Goossens, L.-J. Li, H.-S. P. Wong, F. H. Koppens, *Nature* **2019**, *573*, 507; h) M. C. Lemme, D. Akinwande, C. Huyghebaert, C. Stampfer, *Nature Communications* **2022**, *13*, 1.

[4] a) C. R. Dean, A. F. Young, I. Meric, C. Lee, L. Wang, S. Sorgenfrei, K. Watanabe, T. Taniguchi, P. Kim, K. L. Shepard, *Nature Nanotechnology* **2010**, *5*, 722; b) L. Britnell, R. Gorbachev, R. Jalil, B. Belle, F. Schedin, A. Mishchenko, T. Georgiou, M. Katsnelson, L. Eaves, S. Morozov, *Science* **2012**, *335*, 947; c) T. Georgiou, R. Jalil, B. D. Belle, L. Britnell, R. V. Gorbachev, S. V. Morozov, Y.-J. Kim, A. Gholinia, S. J. Haigh, O. Makarovsky, *Nature nanotechnology* **2013**, *8*, 100.

[5] a) S. M. Sze, Y. Li, K. K. Ng, *John Wiley and Sons* **2021**; b) S. Sze, K. K. Ng, *John Wiley and Son* **2006**, *3*; c) R. T. Tung, *Applied Physics Reviews* **2014**, *1*, 011304; d) Y. Liu, J. Guo, E. Zhu, L. Liao, S.-J. Lee, M. Ding, I. Shakir, V. Gambin, Y. Huang, X. Duan, *Nature* **2018**, *557*, 696.

[6] a) T. Shen, J.-C. Ren, X. Liu, S. Li, W. Liu, *Journal of the American Chemical Society* **2019**, *141*, 3110; b) N. F. Mott, *Proceedings of the Royal Society of London. Series A. Mathematical and Physical Sciences* **1939**, *171*, 27.

[7] S. Banerjee, L. Cao, Y. S. Ang, L. Ang, P. Zhang, *Physical Review Applied* **2020**, *13*, 064021.

[8] a) F. Zhang, W. Li, Y. Ma, Y. Tang, X. Dai, *RSC advances* **2017**, *7*, 29350; b) Y. Wang, M. Chhowalla, *Nature Reviews Physics* **2022**, *4*, 101.

[9] a) B.-K. Kim, T.-H. Kim, D.-H. Choi, H. Kim, K. Watanabe, T. Taniguchi, H. Rho, J.-J. Kim, Y.-H. Kim, M.-H. Bae, *2D Materials and Applications* **2021**, *5*, 1; b) B.-K. Kim, D.-H. Choi, T.-H. Kim, H. Kim, K. Watanabe, T. Taniguchi, H. Rho, Y.-H. Kim, J.-J. Kim, M.-H. Bae, *arXiv preprint arXiv* **2019**, *1904*, 10295; c) D. H. Choi, H. Ji, G. H. Han, B. H. Moon, Y. H. Lee, *Physical Review Applied* **2022**, *18*, 014068.

[10] P. V. Pham, S. C. Bodepudi, K. Shehzad, Y. Liu, Y. Xu, B. Yu, X. Duan, *Chemical Reviews* **2022**, *122*, 6514.

[11] W. Feng, W. Zheng, W. Cao, P. Hu, *Advanced materials* **2014**, *26*, 6587.

[12] W. Feng, X. Zhou, W. Q. Tian, W. Zheng, P. Hu, *Physical Chemistry Chemical Physics* **2015**, *17*, 3653.

[13] J. Kim, A. Venkatesan, N. A. N. Phan, Y. Kim, H. Kim, D. Whang, G. H. Kim, *Advanced Electronic Materials* **2022**, *8*, 2100941.

[14] A. Parappurath, S. Mitra, G. Singh, N. K. Gill, T. Ahmed, T. P. Sai, K. Watanabe, T. Taniguchi, A. Ghosh, *Physical Review Applied* **2022**, *17*, 064062.

[15] K. Stokbro, M. Engelund, A. Blom, *Physical Review B* **2012**, *85*, 165442.

[16] a) J. Kang, D. Sarkar, W. Liu, D. Jena, K. Banerjee, in *International Electron Devices Meeting* **2012**, 1-4; b) I. Popov, G. Seifert, D. Tománek, *Physical Review Letters* **2012**, *108*, 156802.

[17] J. Kang, D. Sarkar, W. Liu, D. Jena, K. Banerjee, in *2012 International Electron Devices Meeting* IEEE, **2012**, 1, 1-17.

[18] a) J. Kang, W. Liu, D. Sarkar, D. Jena, K. Banerjee, *Physical Review X* **2014**, *4*, 031005; b) J. Kang, W. Liu, K. Banerjee, *Applied Physics Letters* **2014**, *104*, 093106.

[19] L.-Y. Gan, Y.-J. Zhao, D. Huang, U. Schwingenschlögl, *Physical Review B* **2013**, *87*, 245307.

[20] L. Britnell, R. M. Ribeiro, A. Eckmann, R. Jalil, B. D. Belle, A. Mishchenko, Y.-J. Kim, R. V. Gorbachev, T. Georgiou, S. V. Morozov, *Science* **2013**, *340*, 1311.

[21] a) Y. Liu, X. Duan, H.-J. Shin, S. Park, Y. Huang, X. Duan, *Nature* **2021**, *591*, 43; b) D. S. Schulman, A. J. Arnold, S. Das, *Chemical Society Reviews* **2018**, *47*, 3037; c) M. Farmanbar, G. Brocks, *Advanced Electronic Materials* **2016**, *2*, 1500405.

[22] a) M. M. Waldrop, *Nature News* **2016**, *530*, 144; b) Y. Jung, M. S. Choi, A. Nipane, A. Borah, B. Kim, A. Zangiabadi, T. Taniguchi, K. Watanabe, W. J. Yoo, J. Hone, *Nature Electronics* **2019**, *2*, 187; c) S. B. Desai, S. R. Madhvapathy, A. B. Sachid, J. P. Llinas, Q. Wang, G. H. Ahn, G. Pitner, M. J. Kim, J. Bokor, C. Hu, *Science* **2016**, *354*, 99; d) J. F. Sierra, J. Fabian, R. K. Kawakami, S. Roche, S. O. Valenzuela, *Nature Nanotechnology* **2021**, *16*, 856; e) D.-F. Shao, S.-H. Zhang, M. Li, C.-B. Eom, E. Y. Tsymbal, *Nature Communications* **2021**, *12*, 1; f) E. Pomerantseva, F. Bonaccorso, X. Feng, Y. Cui, Y. Gogotsi, *Science* **2019**, *366*, 8285.

[23] a) D. Neumaier, S. Pindl, M. C. Lemme, *Nature Materials* **2019**, *18*, 525; b) M. Si, C.-J. Su, C. Jiang, N. J. Conrad, H. Zhou, K. D. Maize, G. Qiu, C.-T. Wu, A. Shakouri, M. A. Alam, *Nature Nanotechnology* **2018**, *13*, 24; c) E. Cha, M. D. Patel, J. Park, J. Hwang, V. Prasad, K. Cho, W. Choi, *Nature Nanotechnology* **2018**, *13*, 337; d) J. R. Schaibley, H. Yu, G. Clark, P. Rivera, J. S. Ross, K. L. Seyler, W. Yao, X. Xu, *Nature Reviews Materials* **2016**, *1*, 16055; e) A. J. Mannix, B. Kiraly, M. C. Hersam, N. P. Guisinger, *Nature Reviews Chemistry* **2017**, *1*, 1; f) S. Yang, C. Jiang, S.-h. Wei, *Applied Physics Reviews* **2017**, *4*, 21304; g) R. Dong, T. Zhang, X. Feng, *Chemical Reviews* **2018**, *118*, 6189; h) C. Anichini, W. Czepa, D. Pakulski, A. Aliprandi, A. Ciesielski, P. Samorì, *Chemical Society Reviews* **2018**, *47*, 4860; i) J. An, X. Zhao, Y. Zhang, M. Liu, J. Yuan, X. Sun, Z. Zhang, B. Wang, S. Li, D. Li, *Advanced Functional Materials* **2022**, *32*, 2110119; j) Y. Fang, Y. Ge, C. Wang, H. Zhang, *Laser & Photonics Reviews* **2020**, *14*, 1900098; k) X. Xiao, H. Wang, P. Urbankowski, Y. Gogotsi, *Chemical Society Reviews* **2018**, *47*, 8744; l) S. Tongay, *AIP Publishing LLC* **2018**, *5*, 10401; m) M. Marian, D. Berman, D. Nečas, N. Emani, A. Ruggiero, A. Rosenkranz, *Advances in Colloid and Interface Science* **2022**, *3*, 102747; n) F. Yi, H. Ren, J. Shan, X. Sun, D. Wei, Z. Liu, *Chemical Society Reviews* **2018**, *47*, 3152; o) T. Fan, L. Yan, S. He, Q. Hong, F. Ai, S. He, T. Ji, X. Hu, E. Ha, B. Zhang, *Chemical Society Reviews* **2022**, *1*, 1; p) C. Ashworth, *Nature Reviews Materials* **2018**, *3*, 1; q) W. Yu, K. Gong, Y. Li, B. Ding, L. Li, Y. Xu, R. Wang, L. Li, G. Zhang, S. Lin, *Small* **2022**, *18*, 2105383; r) X. Liu, M. C. Hersam, *Nature Reviews Materials* **2019**, *4*, 669; s) M. Macha, S. Marion, V. V. Nandigana, A. Radenovic, *Nature Reviews Materials* **2019**, *4*, 588; t) M. Long, P. Wang, H. Fang, W. Hu, *Advanced Functional Materials* **2019**, *29*, 1803807; u) Z. Dai, L. Liu, Z. Zhang, *Advanced Materials* **2019**, *31*, 1805417; v) X. Zhao, J. Shi, Y. Ji, Y. Liu, *Wiley Interdisciplinary Reviews: Computational Molecular Science* **2019**, *9*, 1418; w) N. R. Glavin, R. Rao, V. Varshney, E. Bianco, A. Apte, A. Roy, E. Ringe, P. M. Ajayan, *Advanced Materials* **2020**, *32*, 1904302; x) W. Du, C. Li, J. Sun, H. Xu, P. Yu, A. Ren, J. Wu, Z. Wang, *Laser & Photonics Reviews* **2020**, *14*, 2000271; y) Z. Hu, Z. B. Liu, J. G. Tian, *Chinese Journal of Chemistry* **2020**, *38*, 981; z) B. Zhang, J. Liu, C. Wang, K. Yang, C. Lee, H. Zhang, J. He, *Laser & Photonics Reviews* **2020**, *14*, 1900240; aa) N. R. Glavin, R. Rao, V. Varshney, E. Bianco, A. Apte, A. Roy, E. Ringe, P. M. Ajayan,

Advanced Materials **2020**, *32*, 1904302; ab) H. Jiang, L. Zheng, Z. Liu, X. Wang, *InfoMat* **2020**, *2*, 1077; ac) A. Rodin, M. Trushin, A. Carvalho, A. Castro Neto, *Nature Reviews Physics* **2020**, *2*, 524; ad) E. Coronado, *Nature Reviews Materials* **2020**, *5*, 87; ae) Z. Li, Y. Lv, L. Ren, J. Li, L. Kong, Y. Zeng, Q. Tao, R. Wu, H. Ma, B. Zhao, *Nature Communications* **2020**, *11*, 1; af) J. Dong, L. Zhang, X. Dai, F. Ding, *Nature Communications* **2020**, *11*, 1; ag) R. Gusmão, M. Veselý, Z. k. Sofer, *Acs Catalysis* **2020**, *10*, 9634; ah) W. Yao, B. Wu, Y. Liu, *ACS Nano* **2020**, *14*, 9320; ai) J. Lipton, G.-M. Weng, J. A. Rhr, H. Wang, A. D. Taylor, *Matter* **2020**, *2*, 1148; aj) Z. Y. Ma Q, Luo D, Or T, Liu Y, Yang L, Dou H, Liang J, Nie Y, Wang X, Yu A. , *Advanced Materials* **2022**, *34*, 2108079.

[24] S. M. Song, J. K. Park, O. J. Sul, B. J. Cho, *Nano Letters* **2012**, *12*, 3887.

[25] L. Wang, I. Meric, P. Huang, Q. Gao, Y. Gao, H. Tran, T. Taniguchi, K. Watanabe, L. Campos, D. Muller, *Science* **2013**, *342*, 614.

[26] Y. Wang, Y. Zhao, X. Ding, L. Qiao, *Journal of Energy Chemistry* **2021**, *60,* 451.

[27] a) Y. Khatami, H. Li, C. Xu, K. Banerjee, *IEEE Transactions on electron devices* **2012**, *59*, 2444; b) *IEEE transactions on electron devices* **2012**, *59*, 2453.

[28] H. Y. Park, W. S. Jung, D. H. Kang, J. Jeon, G. Yoo, Y. Park, J. Lee, Y. H. Jang, J. Lee, S. Park, *Advanced Materials* **2016**, *28*, 864.

[29] T. Chu, Z. Chen, *ACS Nano* **2014**, *8*, 3584.

[30] F. Gao, H. Yang, P. Hu, *Small Methods* **2018**, *2*, 1700384.

[31] J. Kang, D. Sarkar, W. Liu, D. Jena, K. Banerjee, *International Electron Devices Meeting* **2012**, *3*, 1.

[32] in *International Electron Devices Meeting* IEEE, **2012**, 1-17.

[33] W. S. Leong, C. T. Nai, J. T. Thong, *Nano Letters* **2014**, *14*, 3840.

[34] a) Y. Ouyang, J. Guo, *Applied Physics Letters* **2010**, *97*, 263115; b) J. Kang, D. Sarkar, Y. Khatami, K. Banerjee, *Applied Physics Letters* **2013**, *103*, 083113.

[35] a) R. Kappera, D. Voiry, S. E. Yalcin, B. Branch, G. Gupta, A. D. Mohite, M. Chhowalla, *Nature Materials* **2014**, *13*, 1128; b) Y.-C. Lin, D. O. Dumcenco, Y.-S. Huang, K. Suenaga, *Nature Nanotechnology* **2014**, *9*, 391.

[36] F. Gao, H. Chen, W. Feng, Y. Hu, H. Shang, B. Xu, J. Zhang, C. Y. Xu, P. Hu, *Advanced Functional Materials* **2021**, *31*, 2104359.

[37] Y. Wang, J. C. Kim, Y. Li, K. Y. Ma, S. Hong, M. Kim, H. S. Shin, H. Y. Jeong, M. Chhowalla, *Nature* **2022**, *3*, 1.

[38] F. Leonard, A. A. Talin, *Nature Nanotechnology* **2011**, *6*, 773.

[39] K. Banerjee, A. Amerasekera, G. Dixit, C. Hu, *International Electron Devices Meeting. IEDM Technical Digest* **1997**, *4*, 115.

[40] V. Heine, *Physical Review* **1965**, *138*, 1689.

[41] A. Anwar, B. Nabet, J. Culp, F. Castro, *Journal of Applied Physics* **1999**, *85*, 2663.

[42] N. Mott, *Le Journal de Physique Colloques* **1976**, *37*, 301.

[43] S. Das, H.-Y. Chen, A. V. Penumatcha, J. Appenzeller, *Nano Letters* **2013**, *13*, 100.

[44] J. Kang, W. Liu, K. Banerjee, *Applied Physics Letters* **2014**, *104*, 093106.

[45] C. D. English, G. Shine, V. E. Dorgan, K. C. Saraswat, E. Pop, *Nano Letters* **2016**, *16*, 3824.

[46] M. Abraham, S. E. Mohney, *Journal of Applied Physics* **2017**, *122*, 115306.

[47] a) R. Kappera, D. Voiry, S. E. Yalcin, B. Branch, G. Gupta, A. D. Mohite, M. Chhowalla, *Nature materials* **2014**, *13* (12), 1128; b) R. Kappera, D. Voiry, S. E. Yalcin, W. Jen, M. Acerce, S. Torrel, B. Branch, S. Lei, W. Chen, S. Najmaei, *Applied Materials* **2014**, *2*, 92516.

[48] W. A. Saidi, *The Journal of Chemical Physics* **2014**, *141*, 094707.

[49] a) S. Banerjee, L. Cao, Y. S. Ang, L. K. Ang, P. Zhang, *Physical Review Applied* **2020**, *13*, 64021; b) A. Allain, J. Kang, K. Banerjee, A. Kis, *Nature Materials* **2015**, *14*, 1195; c) S. Das, H. Y. Chen, A. V. Penumatcha, J. Appenzeller, *Nano Letters* **2013**, *13*, 100.

[50] Y. S. Ang, H. Y. Yang, L. K. Ang, *Physical Review Letters* **2018**, *121*, 056802.

[51] D. Sinha, J. U. Lee, *Nano Letters* **2014**, *14*, 4660.

[52] Y. S. Ang, H. Y. Yang, L. Ang, *Physical Review Letters* **2018**, *121*, 056802.

[53] E. S. Kadantsev, P. Hawrylak, *Solid State Communications* **2012**, *152*, 909.

[54] a) H. Liu, M. Si, Y. Deng, A. T. Neal, Y. Du, S. Najmaei, P. M. Ajayan, J. Lou, P. D. Ye, *ACS Nano* **2014**, *8*, 1031; b) W. Liu, J. Kang, W. Cao, D. Sarkar, Y. Khatami, D. Jena, K. Banerjee, *IEEE* **2013**, *2*, 1; c) Y. Guo, Y. Han, J. Li, A. Xiang, X. Wei, S. Gao, Q. Chen, *ACS Nano* **2014**, *8*, 7771; d) B. W. Baugher, H. O. Churchill, Y. Yang, P. Jarillo-Herrero, *Nano Letters* **2013**, *13*, 4212; e) D. Kiriya, M. Tosun, P. Zhao, J. S. Kang, A. Javey, *Journal of the American Chemical Society* **2014**, *136*, 7853; f) L. Yang, K. Majumdar, H. Liu, Y. Du, H. Wu, M. Hatzistergos, P. Hung, R. Tieckelmann, W. Tsai, C. Hobbs, *Nano Letters* **2014**, *14*, 6275; g) W. Liu, D. Sarkar, J. Kang, W. Cao, K. Banerjee, *ACS Nano* **2015**, *9*, 7904; h) J. Xiao, Z. Kang, B. Liu, X. Zhang, J. Du, K. Chen, H. Yu, Q. Liao, Z. Zhang, Y. Zhang, *Nano Research* **2022**, *15*, 475; i) M. Farronato, M. Melegari, S. Ricci, S. Hashemkhani, A. Bricalli, D. Ielmini, *Advanced Electronic Materials* **2022**, *1*, 2101161; j) X. Wang, X. Chen, J. Ma, S. Gou, X. Guo, L. Tong, J. Zhu, Y. Xia, D. Wang, C. Sheng, *Advanced Materials* **2022**, *1*, 2202472; k) A. Conde-Rubio, X. Liu, G. Boero, J. r. Brugger, *ACS Applied Materials & Interfaces* **2022**, *3*, 1; l) B. W. Yao, J. Li, X. D. Chen, M. X. Yu, Z. C. Zhang, Y. Li, T. B. Lu, J. Zhang, *Advanced Functional Materials* **2021**, *31*, 2100069; m) S. Song, A. Yoon, J.-K. Ha, J. Yang, S. Jang, C. Leblanc, J. Wang, Y. Sim, D. Jariwala, S. K. Min, *Nature Communications* **2022**, *13*, 1; n) J. Jang, Y. Kim, S.-S. Chee, H. Kim, D. Whang, G.-H. Kim, S. J. Yun, *ACS Applied Materials & Interfaces* **2019**, *12*, 5031; o) S. Zhang, S. T. Le, C. A. Richter, C. A. Hacker, *Applied Physics Letters* **2019**, *115*, 073106; p) N. Li, Q. Wang, C. Shen, Z. Wei, H. Yu, J. Zhao, X. Lu, G. Wang, C. He, L. Xie, *Nature Electronics* **2020**, *3*, 711; q) S. Kc, R. C. Longo, R. Addou, R. M. Wallace, K. Cho, *Scientific Reports* **2016**, *6*, 1; r) S. Conti, L. Pimpolari, G. Calabrese, R. Worsley, S. Majee, D. K. Polyushkin, M. Paur, S. Pace, D. H. Keum, F. Fabbri, *Nature Communications* **2020**, *11*, 1; s) R. Yang, H. Li, K. K. Smithe, T. R. Kim, K. Okabe, E. Pop, J. A. Fan, H.-S. P. Wong, *Nature Electronics* **2019**, *2*, 108; t) B. Radisavljevic, A. Radenovic, J. Brivio, V.

Giacometti, A. Kis, *Nature Nanotechnology* **2011**, *6*, 147; u) Q. Hua, G. Gao, C. Jiang, J. Yu, J. Sun, T. Zhang, B. Gao, W. Cheng, R. Liang, H. Qian, *Nature Communications* **2020**, *11*, 1; v) E. Liu, Y. Fu, Y. Wang, Y. Feng, H. Liu, X. Wan, W. Zhou, B. Wang, L. Shao, C.-H. Ho, *Nature Communications* **2015**, *6*, 1.

[55] S. S. Cohen, *MRS Online Proceedings Library (OPL)* **1982**, *18*, 2.

[56] a) D. B. Scott, W. R. Hunter, H. Shichijo, *IEEE Journal of Solid-State Circuits* **1982**, *17*, 281; b) K. Nagashio, T. Nishimura, K. Kita, A. Toriumi, *IEEE* **2009**, *8*, 1.

[57] C. Weißenfels, P. Wriggers, *Computational Mechanics* **2010**, *46*, 301.

[58] F. Liu, H. Shimotani, H. Shang, T. Kanagasekaran, V. Zólyomi, N. Drummond, V. I. Fal'ko, K. Tanigaki, *ACS Nano* **2014**, *8*, 752.

[59] a) K. T. Butler, D. W. Davies, H. Cartwright, O. Isayev, A. Walsh, *Nature* **2018**, *559*, 547; b) G. Cheon, E. D. Cubuk, E. R. Antoniuk, L. Blumberg, J. E. Goldberger, E. J. Reed, *The Journal of Physical Chemistry Letters* **2018**, *9*, 6967.

[60] F. Xue, C. Zhang, Y. Ma, Y. Wen, X. He, B. Yu, X. Zhang, *Advanced Materials* **2022**, *1*, 2201880.

[61] C.-Y. Wang, S.-J. Liang, S. Wang, P. Wang, Z. a. Li, Z. Wang, A. Gao, C. Pan, C. Liu, J. Liu, *Science Advances* **2020**, *6*, 6173.

[62] Y. Wang, Y. Zhao, X. Ding, L. Qiao, *Journal of Energy Chemistry* **2021**, *60*, 451.

[63] H. K. Ng, A. Abutaha, D. Voiry, I. Verzhbitskiy, Y. Cai, G. Zhang, Y. Liu, J. Wu, M. Chhowalla, G. Eda, *ACS Applied Materials and Interfaces* **2019**, *11*, 12184.

[64] K.-A. N. Duerloo, Y. Li, E. J. Reed, *Nature Communications* **2014**, *5*, 1.

[65] Z. Wang, X. Liu, J. Zhu, S. You, K. Bian, G. Zhang, J. Feng, Y. Jiang, *Science Bulletin* **2019**, *64*, 1750.

[66] M. A. Lukowski, A. S. Daniel, F. Meng, A. Forticaux, L. Li, S. Jin, *Journal of the American Chemical Society* **2013**, *135*, 10274.

[67] Y. Zheng, J. Gao, C. Han, W. Chen, *Cell Reports Physical Science* **2021**, *2*, 100298.

[68] X. Hu, J. Lee, D. Berman, A. Martini, *Carbon* **2018**, *137*, 118.

[69] B.-C. Alloys, *Age* **1990**, *400*, 300.

[70] S. Batool, M. Idrees, M. S. Javed, M. Saleem, J. Kong, *Materials Chemistry and Physics* **2020**, *246*, 122832.

[71] S. Batool, M. Idrees, S. T. Han, Y. Zhou, *Advanced Science* **2022**, 2203956.

[72] T. Iwasaki, K. Endo, E. Watanabe, D. Tsuya, Y. Morita, S. Nakaharai, Y. Noguchi, Y. Wakayama, K. Watanabe, T. Taniguchi, *ACS applied materials & interfaces* **2020**, *12*, 8533.

[73] P. Hou, Y. Lv, Y. Chen, Y. Liu, C. Wang, P. Zhou, X. Zhong, J. Wang, X. Ouyang, *ACS Applied Electronic Materials* **2019**, *2*, 140.

[74] C. Cho, P. Kang, A. Taqieddin, Y. Jing, K. Yong, J. M. Kim, M. F. Haque, N. R. Aluru, S. Nam, *Nature electronics* **2021**, *4*, 126.

[75] H. Yu, M. Liao, W. Zhao, G. Liu, X. Zhou, Z. Wei, X. Xu, K. Liu, Z. Hu, K. Deng, *ACS Nano* **2017**, *11*, 12001.

[76] Y. S. Rim, S. H. Bae, H. Chen, N. De Marco, Y. Yang, *Advanced Materials* **2016**, *28*, 4415.

The physics and materials science of electrical contact resistance in 2D materials-based nanoelectronics, interface configurations, charge injection mechanisms, and numerical modeling of electrical contacts, as well as the most pressing issues that need to be resolved in the field of research and development, are discussed in this article.

Electrical Contacts with 2D Materials: Current Developments and Future Prospects

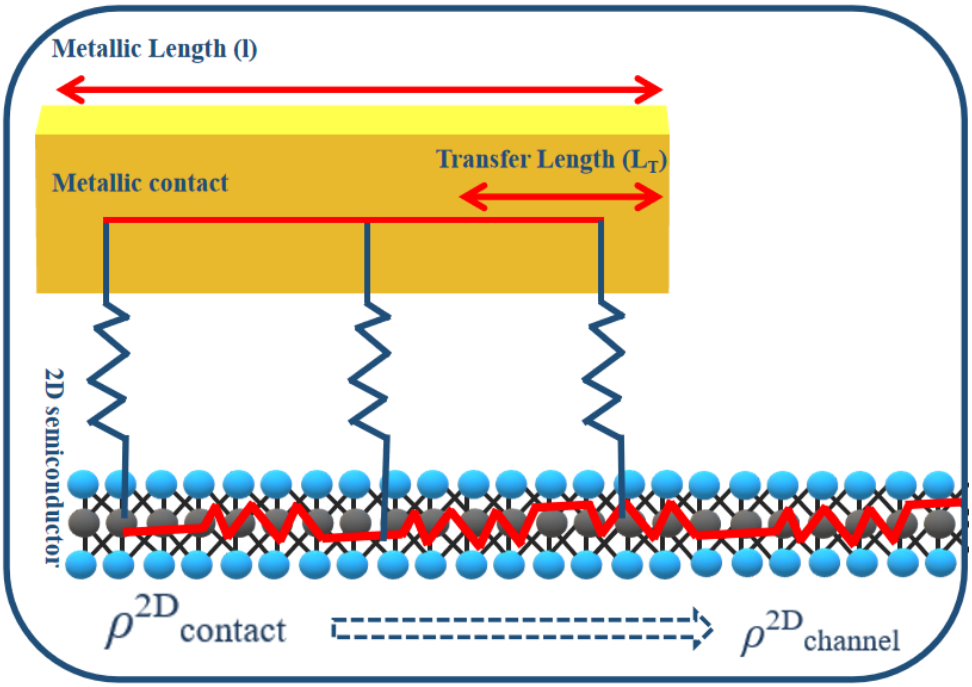

Saima Batool is currently a postdoc candidate in Professor Ye Zhou's group at Institute for Advanced Study, Shenzhen University, China. She received her Ph.D. degree from Northwestern Polytechnical University, China. She is working on the synthesis of nanostructured advanced functional materials and their applications in optoelectronic and electrical devices.

Muhammad Idrees holds a Ph.D. degree in Chemistry from Northwestern Polytechnical University, China. He is now a postdoctoral research fellow at Shenzhen University, China. His current research focuses on multifunctional hybrid materials, especially the preparation and 3D printing of polymer-derived ceramics and their applications in electrical devices.

Su-Ting Han is a professor at Shenzhen University. She received her MSc degree in Analytical Chemistry from Hong Kong Baptist University and her Ph.D. degree in Physics and Materials Science from the City University of Hong Kong. After graduation, she worked at the City University of Hong Kong as a postdoctoral fellow. Her research interests include functional electronic devices and flexible, stretchable, and wearable electronics.

Ye Zhou is a Fellow of the Institute of Physics (FInstP), Fellow of the Royal Society of Chemistry (FRSC), Fellow of the Institution of Engineering and Technology (FIET) and group leader in the Institute for Advanced Study, Shenzhen University. His research interests include organic/inorganic semiconductors, surface and interface physics, and nano-scale devices for

technological applications, such as logic circuits, data storage, photonics, and sensors.